MECHANICAL BEHAVIOR of ALUMINUM-BEARING FERRITIC ALLOYS for ACCIDENT-TOLERANT FUEL CLADDING APPLICATIONS

A Thesis
Presented in Partial Fulfillment of the Requirement for the
Degree of Master of Science
with a
Major in Materials Science and Engineering
in the

College of Graduate Studies

University of Idaho

by

Ankan Guria

Major Professor: Indrajit Charit, Ph.D.

Committee Members: Krishnan Raja, Ph.D.; Batric Pesic, Ph.D.

Department Chair: Eric Aston, Ph.D.

December 2015

Authorization to Submit Thesis

This thesis of Ankan Guria, submitted for the degree of Master of Science with a Major in Materials Science and Engineering and titled "Mechanical behavior of aluminum-bearing ferritic alloys for accident-tolerant fuel cladding applications", has been reviewed in final form. Permission, as indicated by the signatures and dates below, is now granted to submit final copies to the College of Graduate Studies for approval.

Major Professor: _____ Date: _____

Indrajit Charit, Ph.D.

Committee Members: _____ Date: _____

Krishnan Raja, Ph.D.

_____ Date: _____

Batric Pesic, Ph.D.

Department Chair:

_____ Date: _____

Eric Aston, Ph.D.

Abstract

Nuclear power currently provides about 13% of electrical power worldwide. Nuclear reactors generating this power traditionally use Zirconium (Zr) based alloys as the fuel cladding material. Exothermic reaction of Zr with steam under accident conditions may lead to production of hydrogen with the possibility of catastrophic consequences. Following the Fukushima-Daiichi incident, the exploration of accident-tolerant fuel cladding materials accelerated. Aluminum-rich (around 5 wt. %) ferritic steels such as Fecralloy, APMT^{TM} and APM^{TM} are considered as potential materials for accident-tolerant fuel cladding applications. These materials create an aluminum-based oxide scale protecting the alloy at elevated temperatures. Tensile deformation behavior of the above alloys was studied at different temperatures (25-500 ^{o}C) at a strain rate of 10^{-3} s^{-1} and correlated with microstructural characteristics. Higher strength and decent ductility of APMT^{TM} led to further investigation of the alloy at various combination of strain rates and temperatures followed by fractography and detailed microscopic analyses. Serrations appeared in the stress-strain curves of APMT^{TM} and Fecralloy steel tested in a limited temperature range (250-400 ^{o}C). The appearance of serrations is explained on the basis of dynamic strain aging (DSA) effect due to solute-dislocation interactions. The research in this study is being performed using the funds received from the US DOE Office of Nuclear Energy's Nuclear Energy University Programs (NEUP).

Acknowledgements

It has been my proud privilege to work with Prof. Indrajit Charit, who has given me ample opportunity to meet the objectives of the present work. I will always remember his constant support, encouragement, important suggestions and valuable comments; in every aspect of the work he has played a great role that has sustained me and allowed me to present this research work in the present form. He took time to keep me focused and motivated with regular grilling and basting. Dr. Charit not only supported me in my academic pursuit but also helped immensely to settle and work in a different culture.

I like to thank Prof. Krishnan Raja and Prof. Batric Pesic for their academic guidance all the time. I gratefully acknowledge The Department of Energy, USA and University of Idaho, for funding my research work with a handsome scholarship. I thank The Graduate and Professional Students' Association for awarding me travel grants for presenting my work at conferences, FiMPART 2015 and MS&T 2015 as well as travelling to CAES, Idaho Falls.

I am indebted to Dr. Somayeh Pasebani, former PhD student of the Chemical and Materials Engineering Department, University of Idaho for helping me with TEM sample preparation at the onset of my research work. Thanks are due to Dr. Kalyan Chitrada and Samuel Madeira for lending me support with microscopy.

I sincerely thank Dr. Sandip Ghosh Chowdhury, National Metallurgical Laboratory, India. Without his help, encouragement and unfailing support it would not have happened for me to reach Idaho and complete my research here. His mentoring and constant enthusiasm helped me overcome the hard times and directed me towards the right decisions. I am indebted to Prof. Dinabondhu Ghosh (Jadavpur University, India) for his encouragement to start a MS, without going for the job at Reliance Oil Refinery India.

Last but not the least, I thank all my Indian friends, especially Alaap, Mahalingam, Kushal, Megha, Pavan and Yashashree who always kept me cheerful.

My foundation of strength has come from my parents and my brother, as it has throughout my life. Especially without the inspiration of my mother it won't have been possible for me to reach this stage. It is she who always has faith in me and has supported me all through and in that note I would like to dedicate my thesis to her.

Table of Contents

List of Tables

Chapter II

Chapter IV

Appendix I

List of Figures

Chapter II

Chapter III

Chapter IV

Chapter V

Appendix I

Chapter I
Introduction

Safe, reliable and economic operation of nuclear power reactor fleet has always been a priority for the nuclear power industry of the advanced nations. Continual improvement of technology, including advanced materials and nuclear fuels, remains central to the industry's success. Decades of research and development have produced considerable advancements in technology and have yielded an extensive base of data, experience, and knowledge on light-water reactor fuel performance under both normal and accident conditions. Among the several missions taken up by government agencies as well as private companies putting efforts to optimize economic operations at nuclear power plants while ensuring safety, one of the most important mission is to develop nuclear fuels and claddings with enhanced accident tolerance. Following the earthquake and tsunami in Japan and the subsequent damage to the Fukushima Daiichi nuclear power plant complex in 2011, enhancing the accident tolerance of LWRs became a topic of serious discussion.

Prior to the Fukushima-Daiichi accident, LWR fuel-cladding development was improved to enhance performance in terms of increased burn-up for waste minimization, increased power density for power upgrades and increased fuel reliability. The Fukushima incident highlighted some undesirable performance characteristics of the traditionally used Zr-based fuel cladding system, e.g. accelerated hydrogen production under certain circumstances. Thus, fuel cladding system behavior under design-basis accident and severe-accident conditions became the primary focus for advanced fuels, along with striving for improved performance under normal operating conditions.

Low neutron absorption cross section, relative abundance, low-cost, good corrosion resistance, less pellet-cladding interaction, reasonable high temperature strength and good

fabricability are the most important requirements of a fuel cladding material. Due to improvements over the last six decades, Zr and Zr-based alloys had optimized properties mentioned above. However, there were limitations in using this alloy and its behavior in the reduced coolant atmosphere in accident scenarios started to constrain its use in future. Having gone through more than sixty years of improvement and research, it was assumed that even with huge variation in the composition or processing of Zr-based alloys, important improvement in accident-tolerance properties may be difficult to achieve. So, a search for new accident tolerant fuel cladding materials was inevitable.

Aluminum containing high-Cr ferritic steels are proposed as the next generation fuel cladding material. Presence of desired characteristics like high resistance to irradiation damage, low coefficient of thermal expansion, high thermal conductivity, combination of Cr and Al to provide protection against steam attack, good mechanical properties even at temperatures above operating conditions and more resistance to environmental cracking than austenitic stainless steel are the main reasons for considering ferritic steels as a potential fuel cladding material. Penalties due to high neutron absorption cross section can be avoided by using thin walled tubes and/or enriching the fuel.

Such Al containing high-Cr ferritic steels, e.g. APMT^{TM}, APM^{TM} and Goodfellow Fecralloy, were procured for our current study. Tensile tests were carried out at a strain rate of 10^{-3} s^{-1} in a temperature range of (25-500 ^{o}C), as the working temperature range of fuel-cladding of LWRs (320-420 ^{o}C) falls within that range. Mechanical properties obtained from the stress-strain curves of these steels were compared with a nuclear grade C35MN steel which is found to be promising from the researched carried out by the Oak Ridge National Laboratory (ORNL).

Comparative results showed APMT^{TM} as a potential material, too. So, further investigation was performed on this alloy.

Serrated flow was observed in the stress-strain curve of this alloy. As these serrations appeared in the tensile tests carried in the service temperature range of LWRs, it was of interest to the current study too. Tensile tests were carried out at other strain rates (10^{-4} and 10^{-2} s^{-1}) to find out the strain-rate and temperature combinations where serrations are observed for this steel. Serrated flow was ascribed to dynamic strain aging (DSA) due to the repeated locking and unlocking of dislocations by solute atmospheres. Characteristic features of DSA such as plateau/peak in yield and tensile strength as a function of temperature, ductility minima and negative strain rate sensitivity were also observed. Activation energy for appearance and disappearance of serration was calculated and it was concluded that the DSA effect was due to interactions between mobile dislocations and interstitial solute atoms whose mobility was affected by the presence of high concentration of substitutional solute atoms. Microstructural investigation of the steel was done in as received condition and after deformation at 300 ^{o}C to understand the deformation mechanism at elevated temperature. Fractography was done on the fracture surfaces of the deformed samples to understand the nature of fracture and the effect of temperature and strain rate on them. Transmission electron microscopy (TEM) and electron backscatter diffraction (EBSD) were done to support the results of tensile test and proposed deformation mechanism.

In a nutshell, the present study attempts to understand the mechanical properties supported by tensile tests and microstructural investigation of an Al-rich high chromium steel, APMT^{TM} at elevated temperature. However, to establish APMT^{TM} as a potential fuel cladding material in LWRs, a comparative study was done with a few more similar alloys.

Chapter II provides the reader with a literature review on accident tolerant fuel-cladding materials and dynamic strain aging. An introduction to fuel cladding is given, followed by a short discussion on loss-of-coolant-accident and reactor design and historical perspective of LWR design and a detailed insight into core degradation process. Some information on Zr-based alloys as a fuel cladding material, its high temperature applications and its performance in reduced coolant atmosphere and its reaction with water are given. Following that, the motivation for exploring alternative fuel cladding materials, the gradual development of alternative accident tolerant fuel cladding materials and the reasons for considering Fe-Cr-Al alloys as a potential replacement to traditionally used Zr-based alloys are discussed. As these alloys show dynamic strain aging at intermediate temperature ranges which fall in the service temperature range of the LWRs, the second part of literature review throws some light on dynamic strain aging. The topics discussed in brief under this part include the phenomena of strain aging in steels, DSA in steel, causes behind DSA, types of serrations observed in DSA, modelling of DSA, various methods for calculation of activation energy for appearance and disappearance of serrations and manifestation of DSA.

Chapter III contains a paper titled "Observation of serrated flow in APMT^{TM} steel" published in Materials Letter, Vol. 160 in July 2015. The paper is the first ever published observation of serrated flow in APMT^{TM} steel, gives an idea of the strength and ductility properties in the intermediate temperature range and provides a preliminary mechanistic insight into the DSA effect in APMT^{TM} steel.

Chapter IV contains a manuscript titled "Tensile properties of accident-tolerant aluminum-bearing ferritic steels" submitted to "Annals of Nuclear Energy" journal and is currently under review. This paper reports the tensile behavior of APMT^{TM} steel over a

temperature range from room temperature to 500 ^{o}C at three strain rates (10^{-4}, 10^{-3} and 10^{-2} s^{-1}).

Chapter V highlights the comparison of tensile properties among the different Fe-Cr-Al alloys. The high strength of APMT^{TM} as seen from tensile stress-strain curves was established with microstructural characterization e.g. transmission electron microscopy and electron back scattered diffraction.

Appendix I contains a paper titled “Tensile deformation behavior of Al-rich ferritic steels for advanced light water reactors” submitted to be published in the proceedings of an international conference “Frontiers in Materials Processing, Applications, Research and Technology 2015” held in Hyderabad, India from 12-15th June, 2015.

Chapter II
Literature review

The literature review of this thesis consists of two parts:-

Part I: Materials for fuel cladding of light water reactor (LWR)

Part II: Dynamic strain aging in steels

Part I: Materials for fuel cladding of light water reactor

1. Light water reactor: LWRs use light water as the coolant and the moderator, and in many cases as the reflector material. These are typically thermal reactors as they utilize thermalized neutrons to cause nuclear fission of U^{235} atoms.

2. Fuel cladding of a LWR: Almost all the reactors in the United States and a majority in the world are thermal reactors wherein thermal neutrons cause the bulk of the fission reactions. To design a prototype reactor, several design elements need to be flawlessly integrated. The reactor fuel (UO_2) are contained in tubes made of metallic alloys known as fuel cladding. The radioactive fuels could be in metallic, alloy, or ceramic forms. The fuel cladding serves many purposes: it provides mechanical support to the fuel, keeps the fission products from leaving the fuel element, and protects the fuels from corrosion, and efficiently transfer fission-generated heat from the fuel to the coolant.

Cladding materials are used to encapsulate the fuel and separate it from the coolant. The requirements for fuel cladding materials are: (a) low cross section for absorption of thermal neutrons, (b) higher melting point, (c) adequate strength and ductility, (d) adequate thermal conductivity, and (e) corrosion resistance.

3. Loss of coolant accident (LOCA) and reactor design:

3.1 LOCA: The LOCA event starts with a decrease followed by loss of the coolant flow due to a break in the coolant pipe; at the same time the reactor is depressurized and scrammed, reducing the power generation in the core [1]. The fuel starts heating up due its decay heat until the emergency core cooling systems (ECCSs) are activated and the fuel cooling commences. Substantial amounts of heat continue to be generated after the scram. Since the thermal full power levels in commercial LWRs often exceed 3000 MW, in LOCA condition without the circulating coolant, the post-scram decay heat deposited in a reactor core can lead to temperature increase followed by degradation of core. Following the Three Mile Island LOCA, numerous operational design changes were incorporated in LWRs in 1980s, which appreciably reduced the probability of core degradation during a severe accident. These design features and upgrades were associated with maintaining core cooling when primary cooling system becomes dysfunctional. In recent times, accidents at Fukushima-Daiichi reactors in Japan following the earthquake and tsunami in 2011 have triggered further research in developing new reactor systems which are more tolerant to accident conditions. Attention is given to improve the safety of LWRs under design-basis (DB) and beyond-design-basis (BDB) accident scenarios. The following discussion throws some light on the core degradation under DB and BDB accident scenarios and possible remedies to mitigate such situations.

3.2 Historical perspective: During the earlier decades of commercial nuclear reactor design, it was believed, given a deterministic analytical approach, that the probability of an accident scenario crossing the safety design limits would be negligible. So, the regulatory authorities for the safety design requirements did not require mitigation strategies for BDB accident scenarios.

The design features of these reactors were based on evaluations of the engineering performance of the fuel/cladding system under accident conditions [2]. So, the basis for current framework of safety regulations of a nuclear reactor design was postulated considering two DB accidents as bounding events: LOCAs and reactivity initiated accidents (RIAs). As an example the design of ECCS was primarily for the purpose of sufficient cooling to prevent cladding and fuel from reaching high temperatures under LOCA conditions.

The partial meltdown of the core at Three Mile Island sparked two important shifts in reactor safety system design assessment and implementation approaches: a) Augmentation of deterministic approach with probability risk assessment (PRA) to capture the complexities of system behavior and b) Transition from active safety systems towards passively safe nuclear reactor concepts. Only a few (~80+) of the recently developed reactors adopt partially passive safety concepts such as Westinghouse AP1000 and GE-Hitachi ESBWR. It is believed that passive safety features and accident tolerant fuels (ATF) combined, can reduce the capital and operating costs, too.

BDB accident scenarios like that of Fukushima-Daiichi incident have challenged the outcomes of the current PRA models used to quantify operational risk for the current operating fleet of reactors of older generation designs. Specific modelling assumptions regarding the event probabilities impacting the overall probabilistic results is the primary issue. The large energy released from the LWR cores due to physical and chemical degradation in a high-temperature steam environment under BDB conditions is the most prominent consequence of aforementioned drawbacks. Thus, current focus is on the core degradation phenomena has sparked a renewed interest in enhancing safety margins by utilizing ATFs.

3.3 Core degradation processes: Fig 1 exhibits the variation of cladding temperature with time under limited coolant conditions. The diagram provides an overview of core degradation phenomena during LOCA and shows the potential for ATF cladding concepts to change the rate of accident progression. There are three phases during LOCA: Lead Up, Mid-Phase and Late-Phase. During Lead Up, loss of water coolant due to pipe break or loss of cooling capability due to pump failure leads to loss of core cooling capability. This phase can last for seconds, minutes or hours in the case of small-break LOCA, large-break LOCA or Station Blackout (SBO), respectively. Further, the remaining coolant in the core is boiled off by the decay heat in the core and the stored energy in the fuel. The temperature rises higher, and when it reaches ~800 ^{o}C, the Mid-Phase sets in. The currently used UO_2-Zr alloy fuel system catastrophically breaks down around this temperature as the fuel rods burst, releasing some radioactive products to the surroundings. Extensive studies on the UO_2-Zr alloy fuel system [3, 4] have shown that oxidation and detrimental interactions (e.g., low melting point eutectic phase formation) accelerate during this phase. In a design basis LOCA, once core depressurizes in the Lead Up phase, coolant is injected into the core and the fuel is quenched by the ECCS. If the ECCS fails due to pump failure, steam and 20-60 tons of Zr alloy in the core reacts along with other reactive components (e.g. control rod constituents, usually Cd) forming hydrogen gas and large amount of heat. This heat (-586 kJ/mol of Zr [5]) is often more than the decay heat, and it exacerbates the degradation process inside the core and rapid production of hydrogen. The temperature then goes up to ~1500 ^{o}C and severe degradation starts leading to the onset of the Late Phase. Following this, hydrogen may cause explosions damaging the outer containment of the nuclear reactor leading to the release of radionuclides to the atmosphere.

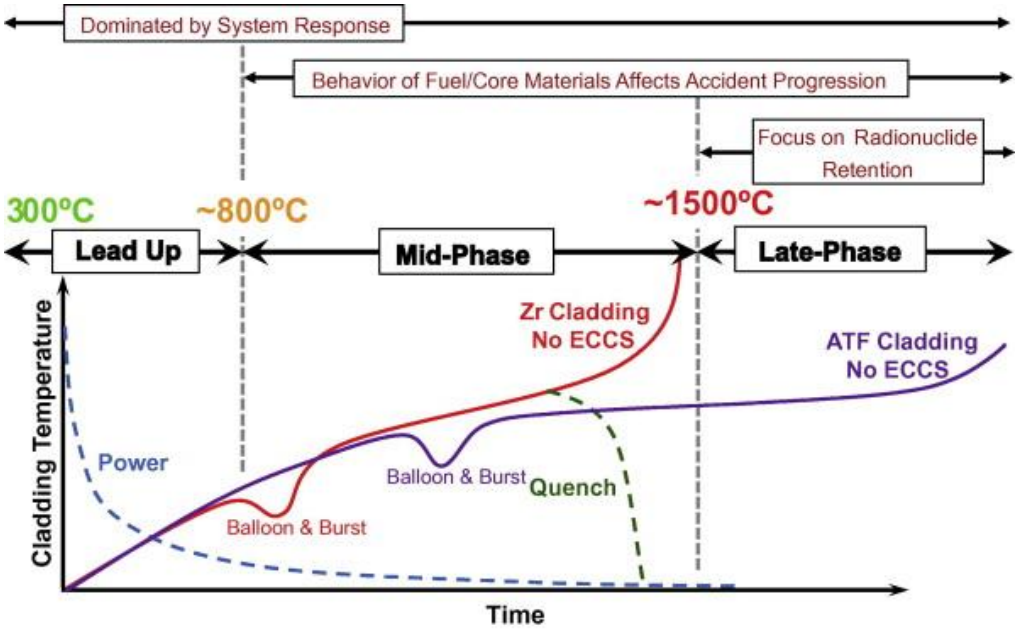

Fig 1: General overview of coolant–limited accident progression inside an LWR core (Directly taken with permission from Journal of Nuclear Materials, 448 (2014), Page 375)

4. Zr-based alloys as a fuel cladding material:

4.1 History: Zr-based alloys are commonly used in water reactors for cladding UO_2. Zircaloy-2 and Zircaloy-4 are used in boiling water reactors (BWR) and pressurized water reactors (PWR), respectively. The historical development of these cladding materials is discussed in the following sections.

Table 1 displays the values of cross section for absorption of thermal neutrons (normalized to Be) and the melting point of various metals:

Be, Mg, Al have low cross sections for absorption of thermal neutrons, but other factors become impediment for their use in commercial reactors. Though Be has a high melting point (1278 ^{o}C), it is scarce, expensive, difficult to fabricate, and toxic. Mg has a low melting point (650 ^{o}C) but has poor high temperature strength and corrosion resistance. Though an Al-based

alloy has been used as fuel cladding materials in reactors like ATR, and Mg-based alloy in Magnox reactors, their use remains limited.

Table 1: Comparative values of cross section for absorption of thermal neutrons and melting point of some metals

Metal	Cross section for absorption of thermal neutrons	Melting point (^oC)
Be	1	1283
Mg	7	650
Zr	20	1845
Al	24	660
Nb	122	2415
Mo	278	2625
Fe	281	1539
Cr	322	1890
Cu	410	1083
Ni	512	1455

So, zirconium-based alloys are the mainstay of fuel cladding materials for LWRs. Apart from low cross section for absorption of thermal neutrons, the favorable features that enable its use as a fuel cladding material are: (a) relative abundance, (b) not prohibitively expensive, (c) good corrosion resistance, (d) reasonable high temperature strength, and (e) good fabricability. Properties are further improved through appropriate alloying. Thus, while all of Al, Be, Mg and Zr have low neutron absorption cross section for thermal neutrons, stainless steels have the best stability under heat and radiation, superalloys (Ni-based) provide the best mechanical strength and refractory metals like Mo, Nb, Ti and W can enhance the high temperature resistance and good heat transfer properties, Zr-based alloys were found to be a material with a balanced combination of all the above properties.

Processing of Zr metal from ore requires removal of hafnium (Hf) which is always associated with Zr in nature. Since Hf has relatively high absorption cross section of thermal neutrons, it is removed from Zr through the expensive Kroll's process (Mg treated) to achieve neutron economy. While O, Sn, Fe, and (Cr, Ni) are added as alloying elements for increasing strength, Cr, Ni and Fe are added for enhancing corrosion resistance. Thus, the Zircaloys were developed (mainly from the US Navy in 1950s under the tutelage of Admiral Rickover).

Sn, Ta and Nb (in decreasing order of effectiveness) were the primary elements chosen for alloying with Zr in fuel cladding application for reactors as they circumvent damaging effects of impurities like N_2 and also improve corrosion resistance. Sn was the first element to be alloyed to produce Zircaloy-1 [2.5Sn-Zr (wt. %) alloy] since neutron economy is affected little and also provided improved corrosion resistance, strength and fabricability. However, breakaway transition in corrosion was not improved. Zircaloy-2 is a 1.5Sn-0.12Fe-0.1Cr-0.05Ni-0.01O-Zr (wt. %) alloy developed in Bettis labs and is used in BWRs. Though Sn content was reduced to 1.5%, it was enough to counteract the nitrogen effect. The strength of Zircaloy-2 was as good as that of Zircaloy-1 but with improved corrosion resistance. Zircaloy-3 was a 0.25Sn-0.25Fe-Zr (wt. %) alloy but was abandoned due to its poor mechanical strength. In this alloy, Sn was further reduced to 0.25% due to its long-term corrosion effect under PWR conditions and Fe was added. However, the understanding of the effects of hydrogen on mechanical properties was just emerging and zirconium hydrides resulted in reduced impact energy. The effect of Ni on hydrogen absorption triggered the development of a new alloy again. PWRs mainly use Zircaloy-4 (1.5Sn-0.21Fe-0.1Cr-0.01C-Zr alloy) (wt. %) where Ni was removed to decrease hydrogen pickup and was replaced by Fe to compensate for the corrosion and strength losses due to removing of Ni.

There were some recent developments in Zr-based alloys:

- Barrier Cladding Zircaloy-2 with Zr liner (inner diameter) for pellet cladding interaction (PCI) resistance
- Zirlo (by Westinghouse): Zircaloy-4 + 0.5 to 1% Nb (by wt.) for good long-term corrosion
- Duplex alloy: Low Sn on the surface (outer diameter) but still in ASTM specification
- Zr + Fe liner in lieu of Zr
- Zr-2/Zr/Zr-2 Triclad

4.2 Science of Zirconium: Zirconium, the prime fuel cladding material in light water reactors is unique among all materials used in LWRs as they have hexagonal close packed (HCP) crystal structure at temperatures <865 ^{o}C (α-Zr). Above that temperature, Zr has a BCC (β-Zr) structure; thus Zr exhibits polymorphism.

The HCP structure in the normal working temperature range of Zr results in significant preferred orientation (texture) during fabrication, which results in anisotropy in properties. Deformation in unirradiated zirconium alloys takes place mainly on prism planes.

4.3 High temperature applications of Zr: Considering the performance of Zircaloy-2 and -4 and Zr-2.5Nb alloys in presently operating reactors, it is very unlikely that any other metal or alloy can surpass these in terms of high temperature corrosion and low neutron absorption cross section. However, above 350 ^{o}C the creep strength diminishes and becomes the criterion for its selection. To improve the efficiency and capital cost, the temperature of the coolant tube must

be significantly raised to temperatures above 450 ^{o}C. The prospects for development of zirconium alloys for high temperature applications are quite promising and attempts are being made to develop such alloys in several laboratories for both cladding and pressure tube applications.

4.4 Performance of Zr during loss of coolant accidents (LOCA): The loss of coolant flow decreases heat transfer from the fuel, increases the fuel temperature and causes a significant temperature rise of the cladding [1]. The decrease in pressure within the system causes a hoop stress in the cladding resulting in creep deformation or ballooning of the cladding. Depending on the cladding ductility and the rod internal pressure, the cladding will either stay intact or burst. The extent of the ballooning is also dependent on the fuel clad hydrogen content. Hydrogen decreases the $\alpha/\alpha+\beta$ phase transformation temperature; thus increasing the hydrogen content in the fuel cladding results in loss of ductility followed by more chances of fuel bursts during a LOCA.

The increasing temperature and presence of steam will cause the intact cladding to oxidize on the outer diameter and the burst cladding to oxidize both the OD and ID (two sided oxidation) [1]. The oxidation process at the high LOCA temperature will increase the oxygen and hydrogen content in the cladding, thus reducing the ductility and resistance to rupture. The cladding oxidizes until the ECCS becomes effective and peak cladding temperature (PCT) is reached. The maximum PCT is supposed to be 1200 ^{o}C. The life of the system at PCT is governed by the equivalent cladding reacted (ECR) limit, defined as the total thickness of cladding that would be converted to stoichiometric ZrO_2 from all of the oxygen present in the fuel cladding as ZrO_2 and oxygen in solid solution in the remaining metal phase.

The cladding is susceptible to embrittlement during LOCA as ECCS activation stops the temperature rise and starts to cool the core. In the temperature range of 400-800 ^{o}C which is known as quenching, the water from ECCS reduces the cladding temperature at a rapid rate (1-5 ^{o}C/s) by rewetting the cladding surface. Such a high rate of cooling collapses the vapor film on the cladding OD and initiates cooling by nucleate boiling. Thermal shock due to the sudden change in heat transfer conditions can fracture the cladding at this stage. The oxidation embrittlement process and resulting structure of the cladding after completion of the LOCA cycle is discussed below in a sequence [1]:

- Increasing water and steam temperatures during heat up enhances the reaction rates with the cladding and increases the conversion of the cladding surface into thicker ZrO_2 films.
- LOCA temperature passes the levels of α to β transformation. The resulting structure consists of the growing ZrO_2 layer, a Zr-layer with a high [O] content which stabilizes the α phase and the bulk cladding in β phase.
- The ECCS-initiated quenching process cools the cladding back down through the β to α transformation temperature and the bulk cladding is now retransformed from β to α phase. This newly formed α phase is also called ‘prior or former β phase’.

Oxygen and hydrogen affect the formation of the structure as follows during oxidation of zirconium:

- Oxygen diffuses from the ZrO_2 to the bulk cladding which is in the β phase at the high temperature; however, the β phase has very low solubility for oxygen. The excess oxygen stabilizes α phase.

- Increased hydrogen levels due to oxidation reaction of Zr prior to and during LOCA increase the diffusion rate and the solubility of oxygen in the β phase > 1000 ^{o}C

4.5 Hazards of metal-water reaction: Although the probability of occurrence is very less in normal reactor operation, under certain conditions, Zr can react with water (or steam) violently resulting in explosions. Such conditions occur during LOCA. The rate of Zr-H_2O reaction depends on the heat of reaction, rate of reaction, specific area of metals, mixing reactants, total quantity of metal, subsidiary heat, such as from combustion of product hydrogen. From the view of reactor environment, most important condition is metal-particle size. Core meltdown can produce particle sizes in the dangerous range, and depending on the core geometry and heat transfer characteristics, the reaction could be self-propagating. The problem was studied by some investigators [6 – 8], and all agree that this phenomenon requires a careful study in each reactor.

5. Motivation for exploring alternative fuel cladding materials:

Rapid fuel pellet expansion against the cladding causing fuel cladding failure and fuel dispersal is the chief concern for the case of reactivity initiated accident conditions. Cladding embrittlement due to radiation damage, and loss of sound metal and formation of hydrides is one of the many issues leading to fuel failure [9]. Zinkle et al. [2] has suggested new cladding systems with improved strength and ductility compared to Zr alloys as one of the potential aspects of accident tolerant fuel systems. Thus, apart from the obvious domination of operational failures of ECCS during LOCA, the Mid Phase phenomena involving exacerbated physical degradation of core and chemical interactions between core constituents (especially

steam and cladding system) also contribute significantly to the progress of accident during limited coolant conditions. Thus, ATF concepts aim to delay the onset of detrimental processes by reducing the high temperature oxidation rate and delaying the ballooning and bursting of the cladding. This will also reduce the burden on the reactor safety systems managing the accident response.

The performance of UO_2-Zr alloy system has already been optimized over the past ~60 years of development. Although further improvements may be anticipated in the Zr alloy cladding, dramatic improvements in accident tolerance is unlikely. Hydride formation in Zr alloy cladding system during operation to high burnups causing loss of sound metal and degradation of toughness will ultimately limit fuel lifetime under normal operating conditions as well as affecting LOCA, RIA and used fuel disposition (UFD) behavior [10 - 12].

The four main desired attributes of ATFs are minimization of core enthalpy input, minimization of combustible hydrogen generation, improvement of fuel containment of fission products and improved cladding to maintain core cooling capabilities and retention of fission products. For LOCAs and SBOs suppression of oxidation of the cladding material in presence of hot steam would minimize hydrogen generation as well as enthalpy input. Additionally, an ideal accident tolerant fuel system should have good dimensional stability i.e., good tensile and thermal creep strength to maintain the core geometry at excess temperatures (~1200 ^{o}C) preventing release of radioactive fission products into the surroundings. For RIA scenarios that increases the temperature in short duration, cladding materials with improved ductility and toughness at moderate to high temperatures along with improved oxidation resistance at normal operating temperatures in comparison to the traditionally used Zr alloys, are required to resist

cladding rupture via pellet-cladding mechanical interactions. Under this situation, the search for alternative accident tolerant fuel cladding materials was inevitable.

6. Development of alternative fuel cladding materials: Thomas [13] described the following characteristics as a requirement for materials for fuel cladding applications at a temperature of at least 450 ^{o}C:

- A minimum stress of 210 to 280 MPa as one third of the ultimate tensile strength (UTS);
- A maximum creep rate of 10^{-7} hr^{-1} after 5,000 hours at a stress of 62 to 74 MPa;
- A minimum of 155 MPa as the stress to rupture in 100,000 hours; and
- A neutron absorption cross section not significantly greater than that of Zircaloy-2.

Zircaloy is traditionally used because of its excellent properties e.g. low neutron absorption (important for maintaining the chain reaction economically), heat transfer properties, and other mechanical properties needed in a material that would be made in to ten- or twelve-foot long thin tubes containing nuclear fuel. The hydrogen generation vulnerability from reaction of Zr with steam, especially during LOCA, has long been recognized since the 1970s well before the 1979 Three Mile Island accident during which there was a hydrogen explosion. Apart from development of oxidation-resistant Zr alloys, application of coatings was taken into consideration. Continuous alloy development efforts over the decades have already improved the high temperature oxidation of Zr alloys. However, the requirement of high temperature oxidation resistance for fuel cladding materials is till 100-fold of the presently used Zr alloy cladding.

Highly adherent oxidation resistant coatings were developed to avoid bulk compositional changes. Possibility of regeneration of small portion of spalled off coating during normal operation or fuel handling would add to the convenience of using such coatings. The major challenges for using a coating were matching of coefficient of thermal expansion of coating and cladding material to minimize interfacial tension stresses leading to delamination and highly anisotropic nature of Zr alloy tubing in the axial versus circumferential directions. Differential volumetric and microstructural evolution between the coating and the cladding material under neutron irradiation can lead to coating spallation, thus leading to oxidation of uncoated portions, hydrogen pickup and cladding embrittlement.

Austenitic stainless steel (ASS) cladding has been recognized as an alternative and has been used in five U.S. light water reactors: Haddam Neck (also known as Connecticut Yankee), Indian Point 1, LaCrosse, San Onofre 1, and Yankee Rowe [14]. ASS reduces but does not eliminate the problem of hydrogen generation, as a similar chemical reaction with steam occurs as with Zr-based alloys. Though ASS cladding was good for pressurized water reactors, their performance in boiling water reactors was poor due to stress corrosion cracking (SCC) problems. Issues to be resolved with ASS were high thermal neutron absorption, SCC, impact of radiation hardening and embrittlement under normal operating conditions and pellet-cladding mechanical interaction behavior under RIA conditions. The use of ASS cladding was stopped in the 1990s after fuel cladding damage was discovered at the Haddam Neck plant; similar damage does not seem to have occurred at San Onofre [15].

There seems to be no readily available drop-in substitute for Zr-based alloys at the present time. It appears that silicon carbide would immensely reduce the problem of hydrogen generation (by one or two orders of magnitude) [16]. Silicon carbide fiber-reinforced SiC matrix

ceramic composites (SiC/SiC) have been proposed for the purpose due to its low thermal neutron absorption cross-section, retention of strength up to very high temperatures, good radiation resistance and good resistance in air and steam up to temperatures as high as 1600 ^{o}C [17,18]. But it has the disadvantages of being brittle. Extensive testing would likely be required for safety and operational reasons before it could be used as a replacement for Zr-based alloys in light water reactors. Generic issues challenging the application of these materials to fuel cladding system are the lack of industry codes and testing standards, lack of familiarity in design and application, development of low cost high performance fibers, development of joining methods and investigation of pellet-cladding mechanical interaction behavior under RIA situations.

The next group of materials that offer potential for significant improvements in high temperature strength compared to Zr based alloys are refractory alloys based on Nb, Ta, Mo, or W. Since these alloys exhibit poor high temperature oxidation resistance [19], techniques for applying adherent oxidation-resistant coatings are under development [20]. Some alloys such as Mo-Si based alloys have, however, shown adequate short term oxidation resistance. Extensive research is being carried out centering monolithic and 'sandwich' designs with refractory alloys in the center and oxidation resistant layers on the inner and outer layers. However, low-cost fabrication of tubing, the effect of higher thermal neutron absorption cross section, impact of radiation hardening, oxidation behavior in steam at high temperature, pellet-cladding mechanical interaction under RIA conditions and cladding embrittlement are some of the challenges to be investigated extensively for using refractory alloys as cladding materials.

7. Proposal for Fe-Cr-Al ferritic alloys: Application of advanced oxidation resistant iron alloys as light water reactor fuel cladding is proposed to compensate for the limitations of traditionally used Zr alloy based fuel cladding under DB and BDB accident scenarios. To minimize penalties in cycle length due to high neutron absorption in the iron based alloys with modest impact on the economics, detailed investigation of mechanical properties and irradiation behavior of these alloys have been coupled with prior experience with cladding materials, leading to approaches involving a combination of cladding thickness reduction and fuel enrichment increase (~0.5%). Recently, extensive research [21–24] have been performed to examine the high temperature oxidation behavior of some iron-based alloys and SiC based materials in 1-20 bar steam. These results were then compared with the benchmarked results of Zr based alloys. Of the materials tested, Kanthal APMT, a ferritic alloy of composition Fe-22.5 wt.%Cr- 5Al-3Mo is the primary focus of our current investigation. This alloy is one example of the class of alumina-forming ferritic alloys that include a wide range of Cr and Al and oxide dispersion strengthened (ODS) variants with enhanced high temperature oxidation resistance. It forms a protective layer of Al_2O_3. Since this protection is inherent to the material, it eliminates th e challenges faced by adherent high temperature oxidation resistant coatings developed for Zr alloys or refractory alloys as discussed above. The chances of mismatch in thermal coefficient, geometrical and dimensional mismatch, ballooning and bursting leading to spallation of the coating are minimized up to large extent in this kind of oxide layer protective coating. For alumina forming Fe-based alloys, the oxide growth kinetics is slower than that of Zr based alloys as the reaction is limited by the diffusion across this layer after 800 ^{o}C, likely by the transport of OH^- ions in steam [25]. Austenitic steels forming Cr_2O_3 could have been a competitor of their ferritic counterparts, but the lesser form stability of Cr-oxide layer in

comparison to the Al-oxide layer due to formation of volatile oxy-hydride limits their applicability [26-28]. Recent research on the oxidation resistance of APMT steel showed that, at 1200 ^{o}C, the degradation of the alloy was nil after 8 hours of exposure to 1000 ^{o}C.

Due to impressive advancements in the use of Zr based alloys as a cladding material for the past few decades, less importance has been given to the Fe-based alloys. However, advanced energy programs have conducted some research on the high corrosion resistant steels. On the basis of already available research results, it appears that these advanced steels would enable development of cladding with thinner walls than that of zirconium alloys, thus mitigating some of the neutronic penalty associated with their use.

In a recent collaborative research carried out by GE Research, University of Michigan and Global Nuclear Fuels, advanced ferritic steels like APMT were declared to have the following desired characteristics favorable to ATF campaign:

1. High resistance to irradiation damage e.g. swelling;
2. Low coefficient of thermal expansion (11.4 μm/m/^{o}C in a temperature range of 0-538 ^{o}C compared to 8.32 or 15.7 of Zircaloy-2 and 18.4 of 304L) and high thermal conductivity (23.9 W/m.K compared to 13.8 of Zircaloy-2 and 16.2 of 304L);
3. Combination of Cr and Al providing protection against attack by steam;
4. Lower cost (in comparison to ASS) due to absence of nickel;
5. Good mechanical properties even at temperatures above operating conditions; and
6. More resistant to environmental cracking than ASS.

Part II: Dynamic strain aging in steels

1. Strain aging in steel: Strain aging of steel was first observed by Bauschinger (1887) when the maximum load carrying capacity of a test piece increased after it was retested after a previous series of testing in the inelastic range. Physical explanation of this phenomenon was interpreted to be time and often, temperature dependent diffusion of small elements such as carbon and nitrogen to crystal defects (e.g. dislocations). Since plastic deformation is triggered by the movement of dislocations through the crystal, the presence of small atoms (e.g. carbon and nitrogen) increases the sliding resistance between the atoms and hence increase the yield strength. Strain aging is of two types: static strain aging (SSA) and dynamic strain aging (DSA).

2. Dynamic strain aging in steel: During deformation of metals and alloys at elevated temperatures, aging processes occur due to interaction of solute atoms and dislocations increasing the necessary stress for the dislocation movement. Solute atoms pin down dislocations raising the yield strength and hardness of the material. Aging occurs slowly at low temperatures because diffusion of the elements responsible for aging is slower. At higher temperatures, diffusion of the solute atoms is facilitated. Dynamic strain aging is the locking of dislocations by solute atoms which easily segregate near the mobile dislocations due to increased diffusivity at higher temperatures. Rodriguez [29] pointed out serrated plastic flow (or abrupt changes in stress observed on stress-strain curves during deformation), negative strain rate sensitivity, maximum in the variation of ultimate tensile strength and strain hardening with temperature, ductility minima in the variation of elongation to fracture as a function of temperature and peak in the variation of Hall-Petch slope with temperature as physical manifestations of DSA. Since strain localization and increased strain hardening rate observed during inhomogeneous plastic flow due to DSA affect the mechanical performance of the

materials, it is important to study the phenomenon and its consequence on materials before putting it into application.

3. Causes of DSA: The basic manifestation of DSA is serrated flow which are instabilities caused by increase in plastic strain. This increase in plastic strain may be due to the following physical processes:-

1. The plastic strain rate under dislocation glide is given by

$$\dot{\varepsilon} = z\rho_m bv \quad (1)$$

where ρ_m is the mobile dislocation density, b the Burgers vector, v the average velocity of dislocations and z is an orientation factor. Serrated flow arises from the increase in ρ_m or v or both.

2. Interaction of moving dislocations with solutes can lead to sudden increase in ρ_m and/or v.
3. Serrations can arise from gradients or modulations in order encountered by moving dislocation in alloys undergoing order-disorder transformations [30-32].
4. Serrations can also be ascribed to mechanical twinning such as those observed in Fe-25 at% Be alloy [33]. Like DSA, twinning is also manifested with positive temperature dependence and a negative strain rate sensitivity.
5. Inhomogeneous plastic flow has been found to occur in tests at cryogenic temperatures for sudden increase in the specimen temperature due to adiabatic heating [34-36]. Load drops due to increase in specimen temperature as heat cannot leave the sample surface as it gets covered with gas molecules of the cryogenic liquid.
6. Stress and strain-induced phase transformations can also cause serrated flow [37].

7. When tested under both hydrostatic pressure and triaxial non-hydrostatic stresses, brittle materials can show serrated flow due to yielding across fracture surfaces [38].

However, the serrations arising from phenomena 4-7 are not ascribed to DSA.

4. Types of serrations: Primarily there are three kinds of prominent serrations whose occurrence is dependent on temperature and strain rate – A, B and C (Fig 2). Type A serrations are predominant at high strain rate and low temperature. They are periodic serrations associated with the repeated initiation and continuous propagation of deformation bands along the specimen gage length. The occurrence of A type serrations has been ascribed to the locking of mobile dislocations by solute atoms on the slip path. Solute atoms at first temporarily arrest dislocations and then form critical atmospheres to lock the dislocations. The abrupt rise of load in the serration is due the increase of stress resulting from pinning of dislocations by the solute atmosphere. The discontinuous load drop signifies the release of dislocations from the solute atmosphere. Type B serration are oscillations about the general level of the stress-strain curve in quick succession. B-type serrations may start from the beginning of serrated yielding at high temperatures and/or low strain rates or may follow A-type serrations with increasing strain. Initiation of such serrations is ascribed to the repeated locking and unlocking of mobile dislocations by highly mobile solute atmospheres [39]. Type C serrations are characterized by yield drops below the mean level of the flow curve and are due to dislocation unlocking. These occur at higher temperatures and lower strain rates than in the case of A and B serrations.

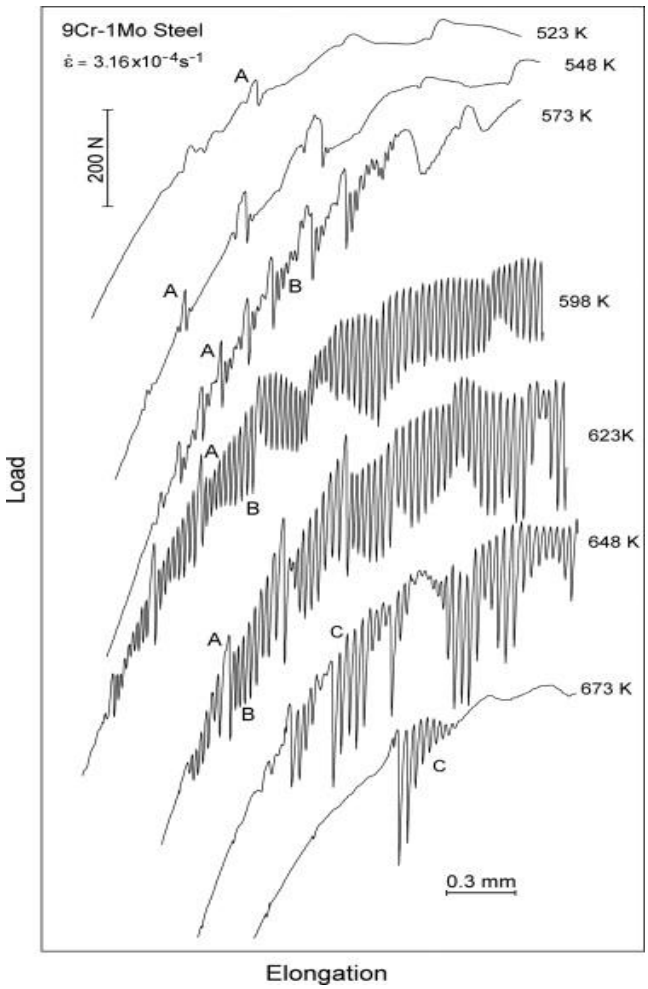

Fig 2: Stress-strain diagram showing the primary types of serrations (A, B and C)
(Directly taken with permission from Materials Science and Engineering A, 564 (2013), Page 306)

Wijler et al. [40] showed D-type serrations in Au-14wt.%Cu alloy for the first time by homogeneous pre-straining at high temperatures. They appear as plateaus in the stress-strain curve due to band propagation like Luders band with no work hardening. E-type serrations are similar to A-type serrations with little or no work hardening during band propagation and occur from A-type serrations at high strain values.

5. Models related to DSA: In a tension test, a specimen is suitably gripped between two cross heads, one moving and the other fixed and deformed at a constant nominal strain rate

determined by the velocity of the moving crosshead. At a certain time, the total strain ε is equal to the sum of the elastic strain ε_e of the specimen-machine system and the plastic strain ε_p of the specimen.

$$\varepsilon = \varepsilon_e + \varepsilon_p \tag{2}$$

$$\dot{\varepsilon} = \dot{\varepsilon}_\mathrm{e} + \dot{\varepsilon}_\mathrm{p} \tag{3}$$

$$\dot{\varepsilon} = \frac{1}{E}\sigma + \dot{\varepsilon}_\mathrm{p} \tag{4}$$

where E is the elastic modulus of the specimen-machine system. Serrations appear when the plastic strain rate $\dot{\varepsilon}_\mathrm{p}$ exceeds the imposed strain rate $\dot{\varepsilon}$, i.e. load drop occurs when there is a sudden increase in $\dot{\varepsilon}_\mathrm{p}$.

Models or theories formulated for serrated flow should be applicable to the different types of serrations that appear in different alloys under all combinations of temperature, strain and strain rate. A critical strain (ε_c) is required for the onset of serrations. It is to note that ε_c increases with increasing strain rate and decreasing temperature, i.e. at high strain rates and low temperatures where A or B serrations dominate. At low strain rates and high temperatures, ε_c increases with decreasing strain rate and increasing temperature where C type serrations are present. The primary models of DSA exhibit variation of ε_c with T and $\acute{\varepsilon}$ in the low temperature regime (high strain rate) based on the interaction of solute atoms and mobile dislocations.

In 1949, Cottrell and Bilby [41] ascribed the phenomenon of strain aging to diffusion of interstitial solutes to mobile dislocation followed by formation of a solute atmosphere to pin the dislocation followed by the release of dislocations. Cottrell (1953) [42] derived the oldest quantitative model for serrated flow assuming that diffusing solutes interact with quasi-

viscously moving dislocations. Three different approaches have been used in modeling of DSA: the 'solute dragging model', 'arrest model' and 'pair reorientation model'.

In Cottrell's 'solute dragging' model, a solute atmosphere is formed by segregation of solute atoms during dislocation movement. He postulated that this mechanism can operate even at lower temperatures unsuitable for bulk diffusion, as vacancies generated from plastic deformation can facilitate diffusion. Also the average velocity of dislocations decreases with plastic straining due to increase in dislocation density. According to Cottrell model, serrated plastic flow will initiate when:

$$\acute{\varepsilon} = \frac{4b\rho_m C_v D_0}{l} \exp(-\frac{Q_m}{k_B T}) \qquad (5)$$

where έ is the strain rate, C_v is the vacancy concentration, D_0 is the diffusion frequency factor, l is the effective radius of the solute atom atmosphere, b is the Burgers vector, ρ_m is the density of mobile dislocations, Q_m is the effective activation energy for solute migration, T is the temperature in K, k_B is the Boltzmann's constant.

Vacancy concentration may increase due to rise in temperature as well as plastic deformation. Similarly, dislocation density may increase due to deformation. Both these increases can be related to plastic strain as:

$$C_v = K\varepsilon^m \quad \text{and} \quad \rho_m = N\varepsilon^\beta \qquad (6)$$

where K, m, N and β are material constants.

In the solute drag regime, the drag force is said to be maximum when the dislocation proceeds at:

$$v_c = \frac{4D_0}{l} \quad (7)$$

Expressing this speed in terms of strain (substituting Equation 7 in Equation 1):

$$\dot{\varepsilon} = \rho_m b v_c = \frac{4b\rho_m}{l} D_0 = \text{AD} \quad (8)$$

Critical strain (ε_c) to initiate DSA is also a function of strain rate and temperature and is given by

$$\varepsilon_c^{m+\beta} = \frac{l\dot{\varepsilon}}{4bKND_0} \exp\left(\frac{Q_m}{k_B T}\right) \quad (9)$$

where m and β are the respective exponents in the relations for the variations in vacancy concentration in Equation 6.

McCormick in 1972 [43] has found that the above equation often yields wrong values of activation energy by several orders of magnitude. However, the equation was the first basis for qualitative understanding of the dependence of ε_c for onset of serration on temperature and strain rate. Moreover, the solute drag model failed to explain the effect of solute concentration on ε_c or on DSA.

In the arrest model it is assumed that the movement of dislocation on a slip plane is discontinuous. A dislocation advances freely for a time (t_f) and gets arrested by a dislocation forest or a precipitate for time t_w. Dislocation velocity in this case is given by:

$$v = \frac{L}{t_f + t_w} \quad (10)$$

where L is the distance between two consecutive obstacles. Depending on temperature, strain rate, strain and diffusion coefficient, the solute concentration may increase pinning down the

dislocations more, hence increasing t_w or may decrease leading to the release of dislocations from the solute atmosphere.

The strain rate at which material can deform due to dislocation glide on the slip plane is obtained by substituting Equation 10 in Equation 8:

$$\acute{\varepsilon} = \rho_m b \frac{L}{t_f + t_w} \tag{11}$$

At critical strain,

$$t_f + t_w = t_a \tag{12}$$

where t_a is the aging time. Friedel (1964) gave an expression for aging time, i.e. the time taken for the diffusing solutes to lock a dislocation:

$$t_a \approx \left(\frac{C_1}{\alpha C_0}\right)^{3/2} \frac{b^2 T k_B}{3D} \tag{13}$$

where C_1 is the concentration of solute required to lock a dislocation, C_0 is the solute concentration of the alloy, α is a constant, D is the solute diffusion coefficient and U_m is the binding energy of solute atom to a dislocation.

Combining equation (11) and (13) and taking $D = C_v D_0 \exp(-Q_m/k_B \mathrm{T})$ yields:

$$\acute{\varepsilon} = \left(\frac{\alpha C_0}{C_1}\right)^{3/2} \frac{3L\rho U_m C_v D_0 \exp(Q_m/k_B \mathrm{T})}{bTk_B} \tag{14}$$

which can then be expressed in terms of critical strain using Equation (9)

$$\varepsilon_c^{m+\beta} = \left(\frac{C_1}{\alpha C_0}\right)^{3/2} \frac{\acute{\varepsilon} k_B \mathrm{T} b \exp(Q_m/k_B \mathrm{T})}{3LNKU_m D_0} \tag{15}$$

Thus, solute concentration around a locked dislocation during serrated flow is a function of arrest time and diffusion coefficient. Keeping the works of McCormick (1972) [43] and Penning (1972) [44] as the basis, Van den Baukel (1975) [45] analyzed in detail all the significant phenomena occurring while DSA.

The pair reorientation model for occurrence of DSA was introduced by Rose and Glover (1966) [46] and based on Snoek (1964) [47] theory. This model shows that the movement of dislocations can be impeded by interactions with solute-vacancy atom pairs.

6. Appearance and disappearance of serrations - Calculation of activation energy: Equation 9 shows the dependence of ε_c on strain rate έ and temperature T. The value of $m + \beta$ can be obtained from the dependence of critical strain on strain rate at a constant temperature. There are several methods for calculating the activation energy for appearance or disappearance of serrations during DSA [39], which are summarized as follows:

1. Method-1: From Equation 9, we can plot ln ε_c vs $1/T$ at a constant strain rate and Q can be calculated as Q = slope × $(m + \beta)$ × k_B [48]. The value of $(m + \beta)$ is calculated as the slope of ln ε_c vs ln έ at constant temperature. This method is called critical strain method and $(m + \beta)$ is evaluated as the average of some values obtained from a combination of strain rates and temperatures.
2. Method-2: In this method, Q can be obtained from the slope of boundaries delineating serrated and smooth flows in ln έ – $1/T$ plot as Q = slope × k_B [49].
3. Method-3: This method, called the intercept method, does not involve the evaluation of $(m + \beta)$ values. From the ln ε_c vs ln έ plots, the intercepts on ln έ corresponding to different critical strains and critical temperatures are obtained. A plot of these intercept

values as ln ἐ vs. $1/T$ corresponding to different critical strains would give a set of parallel lines, whose average slope yield Q as slope × k_B.

4. Method-4: Using Equation 15, Q is calculated for a given ἐ from the plot of ln $\varepsilon_c^{(m+\beta)/T}$ vs. $1/T$ as Q = slope × k_B [50]. $(m+\beta)$ values are obtained at different temperatures.
5. Method-5: Q can also be obtained from the measurement of load drops during serrated flow [51, 52].

In general, the activation energy for appearance of serration is quite similar to that of the activation energy of the diffusing solute species.

7. Effect of composition on DSA in steels: Baird (1973) [53] summarized the manifestations and effects of DSA in mild steels for the first time. In 1968, Keh et al. [58] reported the occurrence of serrated flow in 0.03 wt.% C steel, quenched from 250 ^{o}C, in the temperature range of 50 – 250 ^{o}C at strain rates of 10^{-4} – 10^{-2} s^{-1}. He also showed the dependence of onset of serrated flow on temperature and interstitial concentration. He evaluated the activation energy in 0.03% C steel as 83.7 kJ/mol. In the same year, Clough et al. [54] attributed blue brittleness or loss of ductility to DSA in annealed 4340 steel at 400 – 670 ^{o}C. In 1970, Roberts and Owen [55] deduced that jerky flow in ferrite is probably due to Snoek ordering of interstitial atoms around mobile dislocations. Following year, in 1971, Bergstrom and Roberts explained that jerky flow may also occur due to formation of Cottrell atmospheres around immobile dislocations. Following Baird's (1973) [53] work on strain hardening showing that in ferrite dislocations cannot be pinned sufficiently due to Snoek ordering, it was clearly evident that the jerky flow is due to Snoek ordering but the rise in strain hardening is due to the formation of Cottrell atmospheres around dislocations.

In low-alloy steels (LAS), serrated flow ascribed to DSA was observed during plastic straining at low strain rates ($<10^{-2}$ s^{-1}) in the temperature range of 100 – 350 ^{o}C [56]. Kim and Kang [57] pointed out that the temperature range for appearance of serrated flow depends on the strain rate and microstructure of the steel. The activation energy evaluated by the above researchers were 75 – 85 kJ/mol, which was pretty close to that of already reported values (65 – 85 kJ/mol) by Keh et al. [58]. Li and Leslie (1978) [59] have shown that the activation energy values for onset of serration were insensitive to the microstructure or composition of the steel and only Mn addition may increase the activation energy for onset of serrations. Mn diffuses to form Mn-N and Mn-C pairs, thus increasing the activation energy for onset of serrations. In ferrite, N and C have similar diffusion coefficients and consequently these two elements produce nearly same effects on the DSA in LAS. In general, the effects produced by C and N on DSA is additive. Since N solubility is higher than that of C, it is assumed that N contributes more to the onset of serrated flow. However, Baird [53] has shown that at higher temperatures, when the solubility of C increases it starts to play a vital role and can cause DSA in the absence of N. Therefore, the occurrence of DSA is considered to occur solely by the diffusion of N and C atoms to the dislocations. Since the disappearance of serrations also arises from interaction between solute atoms and dislocations, it is suggested that the activation energy for disappearance of serrations must be equal to the sum of the activation energies for diffusion and binding energy of the interstitial atoms to the dislocations. However the reported high values of activation energy proves that it is a function of composition.

DSA can occur due to the effect of substitutional elements too, but at higher temperatures. At lower temperatures, the diffusivity of substitutional elements is too low to contribute solely to the locking of dislocations. However, in concentrated alloys, the mobility

of interstitial elements can be affected by the presence of substitutional elements, thus raising the activation energy required for onset or occurrence of serrated flow.

The effectiveness of element in contributing to DSA depends on its solubility, diffusivity and severity with which it locks the dislocations. There are two classes of elements on the basis of their participation in DSA effect. The first class elements contribute to DSA by diffusing quickly enough through the lattice to diffuse to the dislocations and locking them e.g. nitrogen and carbon. The second class of elements e.g. Ti, Nb, Mo, Cr influence the mobility of interstitial elements and thus contribute to DSA in steels. While some of them interact with nitrogen and carbon forming nitrides, carbides, etc., others participate in stress-induced ordering of substitutional-interstitial pairs or complexes, thus lowering the mobility of nitrogen and carbon effectively.

Kishore et al. [60] demonstrated that the size of the elements and precipitates can also affect DSA in steels. On examining the behavior of two steels, one treated at a temperature higher than the other, it was found that the steel heated at lower temperature exhibited less serrated flow than the one treated at higher temperature. It was postulated that the finer precipitates acted as more effective carbon sinks than the coarser ones, and therefore deplete the solute atmospheres more rapidly. As plastic deformation proceeds, the segregated solute atoms get depleted from the Cottrell atmospheres formed and slowly diffuse, through pipe diffusion, to the precipitate sinks.

8. Manifestations of DSA: Apart from the appearance of serrations in the stress-strain curve, there are some other obvious manifestations which are expected to occur during DSA. Some

obvious manifestations of DSA are shown in Fig 3. In the figure, K_ε is the Hall-Petch slope, Θ is the work hardening rate, γ is the strain rate sensitivity and other symbols are predefined.

1. Peak or plateau in strength: The strength of the initial obstacle substructure of a material prior to work hardening is the yield stress, σ_{ys} and the corresponding flow stress σ_f is the yield stress of the strain hardened material. The strain hardening contribution $\Delta\sigma$ is calculated as the change in strength that results from plastic deformation and is given as

$$\Delta\sigma = \sigma_f - \sigma_{ys} \qquad (16)$$

There are a number of factors that contribute to the strain hardening effect. The overall work hardening or strain hardening is obtained by

$$\Delta\sigma = \Delta\sigma_{dd} + \Delta\sigma_{dp} + \Delta\sigma_{ds} \qquad (17)$$

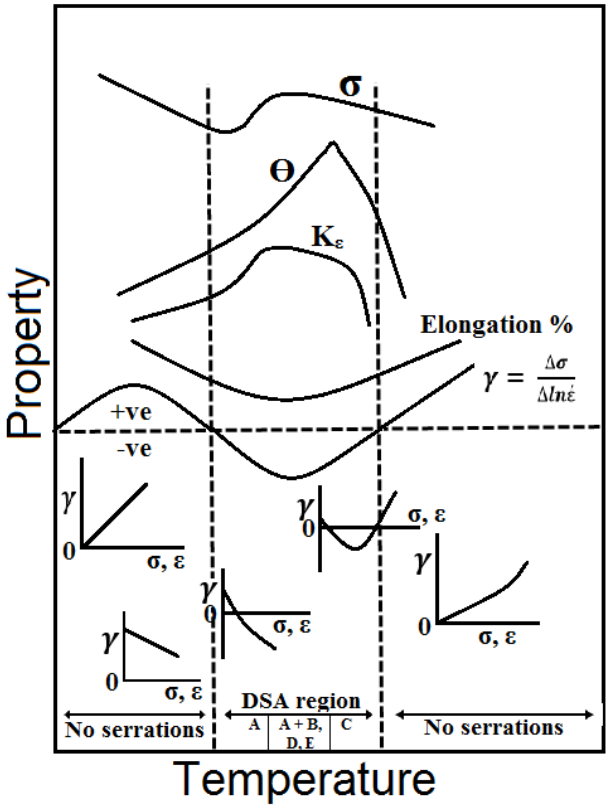

Fig 3: Schematic illustration of the various manifestations of dynamic strain aging (Adapted from Bulletin of Materials Science, V- 6, No. 4 (1984), 661)

where, $\Delta\sigma_{dd}$ stands for increase in flow stress due to dislocation-dislocation interactions, $\Delta\sigma_{dp}$ for dislocation-particle interactions and $\Delta\sigma_{ds}$ for dislocation-solute interactions. $\Delta\sigma_{ds}$ encompasses all other effects during DSA and contributes significantly to the overall work hardening.

A common way of demonstrating the influence of DSA on flow stress of a material is to exhibit the variation of change in magnitude of work hardening with respect to the magnitude of work hardening at room temperature as a function of temperature.

$$\Delta\sigma_a = \Delta\sigma + \Delta\sigma_o \qquad (18)$$

where, $\Delta\sigma_o$ is $\Delta\sigma$ at room temperature (the flow stress, σ_f is generally taken as the UTS or peak stress).

2. Negative strain rate sensitivity: In a normal thermally activated process, the flow stress increases as the strain rate increases. However, in the DSA region, the resistance to motion is raised as the strain rate or dislocation velocity decreases. This is due to the longer time the dislocation spends arrested at obstacles when moving at a low average velocity, which facilitates more segregation of solute atoms around the dislocation. Due to the high solute concentration around the dislocation, there is a strengthening effect and a higher stress is required to move that dislocation. Deformation can occur at a lower stress with an increase in strain rate and can lead to flow localization (or inhomogeneous deformation).

9. Concluding remarks: ATF cladding materials are under primary focus for developing the next generation LWRs to withstand DB and BDB accident scenarios. Ferritic steels are proposed for their near-versatile characteristics required in fuel cladding materials. A few aluminum-rich high chromium ferritic alloys are under research in this thesis. Tensile tests of these alloys at elevated temperature exhibits DSA. DSA occurs due to repeated pinning and unpinning of dislocations due to solutes. Important manifestations of DSA include serrated flow, negative strain rate sensitivity and peak or plateau in the variation of strength to temperature.

References:

1. Strasser A., Garzarolli F., Rudling P., ANT International, Molnlycke, Sweden, 2010b
2. Zinkle, S.J., Terrani, K.A., Gehin, J.C., Ott, L.J., Snead, L.L., J. Nuc. Mater. 448 (2014), 374-379.
3. P. Hofmann, J. Nucl. Mater., 270 (1990), 194
4. M. Steinbrück, M. Große, L. Sepold, J. Stuckert, Nucl. Eng. Des., 240 (2010), p. 1714
5. L. Baker, L.C. Just, ANL-6548, Argonne National Laboratory (1962)
6. D.R.Olander, Concise Encyclopedia of Materials for Energy Systems, J.W.Martin (ed.), Elsevier (2000), 31
7. P.L.Anderson, Mat. Performance and Evaluation, R.H.Jones (ed.), ASM International, materials park, OH (1998), 181
8. D.G.Franklin and R.B.Adamson, J. Nucl. Mater., 159 (1988), 12-21
9. Nuclear Fuel Behaviour under Reactivity-initiated Accident (RIA) Conditions, NEA Report No. 6847, Nuclear Energy Agency, OECD, Paris, 2010
10. Nuclear Fuel Safety Criteria Technical Review, NEA Report No. 7072, second ed., Nuclear Energy Agency, OECD, Paris, 2012
11. K.A. Terrani, S.J. Zinkle, L.L. Snead, J. Nucl. Mater., 448 (2014), 420–435
12. J.-C. Brachet, V. Vandenberghe-Mailliot, L. Portier, D. Gilbon, A. Lesbros, N. Waeckel, J.P. Mardon, J. ASTM Int., 5 (2008), JAI101116
13. Thomas et al., Nuclear Technology, 7 (1969), 144-154
14. DOE 1994: U.S. Department of Energy. Spent Nuclear Fuel Discharges from U.S. Reactors 1992. (SR/CNEAF/94-01) Washington, DC: DOE, Energy Information Administration, Office of Coal, Nuclear, Electric and Alternate Fuels, Survey Management Division, May 1994.
15. J. E. Rivera and J. E. Meyer. Stainless Steel Clad for Light Water Reactor Fuels. (Energy Laboratory Report No. MIT-EL 80-021) Cambridge: EL, Massachusetts Institute of Technology, July 1980
16. Center for Advanced Nuclear Energy Systems. Silicon Carbide Reports. Cambridge, CANES, Department of Nuclear Science & Engineering, Massachusetts Institute of Technology, viewed September 14, 2011.

17. K. Yueh, D. Carpenter, H. Feinroth, Nucl. Eng. Int., 55 (2010), 75–87
18. K. Yueh, K.A. Terrani, J. Nucl. Mater., 448 (2014), 380–388
19. J.H. Schneibel, R.O. Ritchie, J.J. Kruzic, P.F. Tortorelli, Metall. Mater. Trans. A, 36A (2004), 525–531
20. J.H. Perepezko, R. Sakidja, JOM, 62 (2010), 13–19
21. B.A. Pint, K.A. Terrani, M.P. Brady, T. Cheng, J.R. Keiser, Journal of Nuclear Materials, 440 (2013), 420–427
22. T. Cheng, J.R. Keiser, M.P. Brady, K.A. Terrani, B.A. Pint, Journal of Nuclear Materials, 427 (2012), 396
23. B.A. Pint, M.P. Brady, J.R. Keiser, T. Cheng, K.A. Terrani, in: Proceedings of the 8th International Symposium on High Temperature Corrosion and Protection of Materials, Les Embiez, France, 2012
24. K.A. Terrani, J.R. Keiser, M.P. Brady, T. Cheng, G.W. Silva, B.A. Pint, L.L. Snead, High Temperature Oxidation of Silicon Carbide and Advanced Iron-Based Alloys in Steam-Hydrogen Environments, Top Fuel 2012, Manchester, UK, 2012.
25. D. Young, D. Naumenko, L. Niewolak, E. Wessel, L. Singheiser, W. Quadakkers, Materials and Corrosion, 61 (2010), 838
26. E.J. Opila, Trans Tech Publ (2004), 765
27. C. Tedmon, Journal of the Electrochemical Society, 113 (1966), 766
28. D.J. Young, B.A. Pint, Oxidation of Metals, 66 (2006), 137
29. P. Rodriguez, Bulletin of Materials Science, V- 6, No. 4 (1984), 653
30. Mannan, S.L. & Rodriguez, Philosophical Magazine 25 (1972), 673
31. Mannan S.L., Samuel K.G., Rodriguez P., Proceeding of 6^{th} international Conference on Strength of Metals and Alloys, Melbourne, August 1982 (ed) R.C. Giffkins (New York: Pergamon Press) Vol. 2, 637-642
32. Samuel, K.G., Mannan, S.L. & Rodriguez, Acta Metallurgica, Vol. 36: 8 (1988), 2323-2327
33. Bolling, G.F. & Richman, R.H. Acta Metallurgica.,Vol. 13:7 (1965), 709-743
34. Ramachandran, International Conference on metal Science, ICMS, Ranchi (1983)

35. Ramachandran Vm, Baldwin D.H. and Reed-Hill R.E., Metallurgical Transactions 1 (1970), 3011
36. Kubin L.P., Spiesser P. and Estrin Y., Acta Metall. 30 (1982), 385
37. Seetharam V., Bulletin of Materials Science 6 (1984)
38. Weertman J., Can. J. Phys., 45 (1967), 797
39. B.K. Choudhary Mater. Sci. Eng. A, 564 (2013), 303–309
40. A. Wijler, Westrum, Beukel, Acta Metall., 20:3 (1972), 355-362
41. A.H. Cottrell & Bilby, Proceedings of Physical Society A. Vol. 62:1 (1949), 49-62
42. A.H. Cottrell, Philosophical Magazine Series 7. Vol. 44:355 (1953), 829-832
43. P.G. McCormick, Acta Metallurgica. Vol. 20 (972), 351 – 354
44. P. Penning, 1972. Mathematics of the Portevin-le Chatelier effect. Acta Metallurgica. Vol. 20:10. pp. 1169-1175
45. A. van den Beukel, Physica Status Solidi (a), 30 (1975), 197-206
46. K.S.B. Rose & G.C. Glover, Acta Metallurgica. Vol. 14:11 (1966), 1505-1516
47. J.L. Snoek, Physica. 8 (1941), 734–744
48. K.W. Qian, R.E. Reed-Hill, Acta Metall., 31 (1983), 87–94
49. D. Blanc, J.L. Strudel, H.J. McQueen, J.P. Bailon, J.I. Dickson, J.J. Jonas, M.G. Akben (Eds.), Strength of Metals and Alloys (ICSMA 7), Vol 1 Pergamon press, Oxford (1986), 349
50. I.S. Kim, M.C. Chaturvedi, Trans. Jpn. Inst. Met., 28 (1987), 205–212
51. B. Russell, Philos. Mag., 8 (1963), 615–630
52. E. Pink, A. Grinberg, Acta Metall., 30 (1982), 2153–2160
53. J.D. Baird, American Society of Metals (1973), Metals Park, OH, USA, 191 – 222
54. W.R. Clough, L. Jackman, Y.G. Andreev, Journal of Basic Engineering, 90 (1968), 13-20
55. M.J. Roberts and W.S. Owen, Metallurgical Transactions, 1 (1970) 3203-3213
56. J.D. Atkinson and J. Yu, Fatigue & Fracture of Engineering Materials & Structures, Vol. 20:1 (1997), 1-12
57. I.S. Kim and S.S. Kang, International Journal of Pressure Vessels & Piping. Vol. 62:2 (1995), 123-129

58. A.S. Keh, Y. Nakada, W.C. Leslie, Dislocation Dynamics. New York, USA: McGraw-Hill, 1968, 381 – 408
59. C.C. Li and W.C. Leslie, Metallurgical Transactions A, Vol. 9:12 (1978), 1765-1775
60. R. Kishore, R.N. Singh, T.K. Sinha, J. Mater. Sci., 32 (1997), 437–442

Chapter III
Observation of serrated flow in APMT^{TM} steel

"Paper published in Materials Letters"

Ankan Guria and Indrajit Charit
Department of Chemical and Materials Engineering
University of Idaho, Moscow, ID 83844-3024, USA

1. Abstract

Aluminum-bearing APMT^{TM} steel is being considered as a potential fuel cladding material for a novel light water reactor design. Elevated temperature tensile tests were performed with APMT^{TM} steel to examine the basic mechanical behavior. Serrations observed in the temperature range of 523 K to 673 K during tensile deformation of APMT^{TM} within a range of strain rates are attributed to dynamic strain aging (DSA) with negative strain rate sensitivity. The DSA effect was due to interactions between mobile dislocations and interstitial solute atoms whose mobility was affected by the presence of high concentration of substitutional solute atoms.

Keywords: metals and alloys; Fe-Cr-Al; accident tolerant fuel cladding; serrations; dynamic strain aging; structural; light water reactor

2. Introduction

Traditionally, zirconium based alloys are used as fuel cladding materials in light water reactors (LWRs). Exothermic reaction with steam under accident conditions may lead to production of hydrogen with possibility of catastrophic consequences. Hence, the I^{2}S-LWR reactor project [1] is considering an aluminum-rich (about 5 wt.%) ferritic steel as an alternative accident-tolerant fuel cladding material to zirconium-based alloys. This type of material creates

an aluminum-based oxide scale protecting the alloy at elevated temperatures. Kanthal APMT^{TM} is advanced ferritic steel with a composition of Fe-21.5Cr-5.0Al-3.1Mo-0.04C-0.34Si-0.16Mn (wt.%) steel, produced via a powder metallurgy process by Sandvik Inc., and is generally used for making high temperature furnace heating elements. With excellent high-temperature corrosion/oxidation resistance, this steel has the potential of being used as a fuel cladding material for nuclear applications.

In the present work, a preliminary investigation was performed on the influence of strain rate and temperature on serrated flow observed during tensile deformation of APMT^{TM} alloy. While there are high temperature tensile data available above 800^{o}C for this alloy in the open literature [2], the tensile properties of this alloy in the low temperature range are not available. Given that the normal LWR core outlet temperature is around 593 K to 693 K, it is important to study the alloy in this temperature range. However, the experimental campaign designed for the current work included a broader temperature range (298 K to 773 K) to gain further scientific insights into the relevant phenomena.

Earlier, ferritic-martensitic steels such as Grade 9 [3, 4-7] and Grade 91 [8-13] 9Cr–1Mo steel, P9 and P91 [14, 15] and P92 [16] have been reported to exhibit dynamic strain aging (DSA) over the temperature range of 498 K to 693 K. Occurrence of DSA in these steels has been manifested by serrated plastic flow, plateau in yield and tensile strength, negative strain rate sensitivity and ductility minima [8-12]. DSA in the conventional 9Cr–1Mo steel has been attributed to interactions of dislocations with carbon atoms [3, 4-6], and with nitrogen atoms in the modified 9Cr–1Mo steel [8, 9, 12]. On the other hand, Keller et al. [11] suggested that DSA occurs due to carbo-nitrides. Serrations due to DSA have also been characterized by internal

friction in several materials like austenitic stainless steel [17], nickel based superalloy [18], and zirconium–hydrogen alloy [19].

Based on the nature of serrations, A-, B-, C- and D-type of serrations have been reported in earlier experiments with ferritic steels [3-13]. Type A serrations exhibit repeated initiation and continuous propagation of deformation bands along the specimen gage length. Sleeswyk [20] and McCormick [21] in their diffusion-controlled models of DSA attributed the occurrence of A-type serrations to diffusion of solute atoms to freely gliding dislocations. Sharp rise in load occurs when the solute locks dislocations, and the load drops when dislocations unlock from the solute atmosphere. Following A-type serrations, repeated locking and unlocking of dislocations due to highly mobile solutes lead to small B-type serrations about the mean level of loads in load-elongation curves. Type C serrations are oscillations of the load-elongation curve below the mean level of load. Type D serrations occur as plateaus due to band propagation similar to Luders band with not much work hardening or strain gradient ahead of the moving band front [22, 23].

Generally, DSA has been found to be detrimental to tensile ductility, low cycle fatigue (LCF) life and creep resistance of structural components which are causes of concern for structural applications [24]. Hence, the role of DSA occurring in a LWR-specific service temperature range (553–693 K) on the tensile behavior of APMT^{TM} alloy is addressed in this study.

3. Methods

An APMT^{TM} steel rod of 12 mm diameter and 1830 mm length was procured from Sandvik for this study. Round tensile specimens of 25.4 mm gauge length and 6 mm gauge diameter were subjected to tensile tests in the temperature range of 298 – 773 K in air using

nominal strain rates of 10^{-4}, 3×10^{-4}, 10^{-3}, 3×10^{-3}, and 10^{-2} s^{-1}. The tensile specimens were allowed to dwell at the test temperature for 30 min to reach temperature stabilization throughout the specimens before starting elevated temperature tests. Stress–strain curves were established from the load extension data and 0.2% offset yield stress (YS), ultimate tensile stress (UTS) and ductility parameters e.g. elongation to fracture and reduction in area were determined. Variation of these properties as a function of temperature was plotted. Fracture surfaces of the tensile tested specimens were examined by field emission scanning electron microscope (Zeiss Supra 35 VP).

4. Results and Discussion

The steel exhibited serrated flow in the temperature range of 523 K to 673 K. Figure 1a shows the variation in serration types at different strain rates at a temperature of 573 K while Figure 1b shows the different types of serrations at different temperatures for a strain rate of 10^{-3} s^{-1}. The curves were shifted from their respective original positions to avoid overlapping and make the serrations distinct. Lower strain rates like 3×10^{-4} s^{-1} and 10^{-4} s^{-1} exhibited the dominance of A or A+C serrations, whereas at higher strain rates B and D types of serrations appeared. The lowermost curve in Figure 1a shows a stress-strain curve obtained from strain rate jump test. With increase in strain rate from 3×10^{-4} s^{-1} to 10^{-2} s^{-1}, stress values decrease which is against the normal behavior.

Unlike other research works done on serrations in low carbon steels exhibiting appreciable critical strain for the onset of serrations, in APMT^{TM} alloy such serrated flow started almost near the onset of plastic deformation. Interestingly, serrations were observed almost throughout the plastic flow at 573 K for all strain rates. With increase in plastic deformation, denser serrations were observed at this temperature. Relevant activation energy values were

calculated according to a method used by Jenkins and Smith [25]. The activation energy for the onset of serrations was found to be ~142 kJ/mol and that for their disappearance ~212 kJ/mol. Such activation energy suggests that the onset of serrations was likely linked to the migration of interstitial solutes such as carbon whose mobility was substantially affected by the substitutional solutes (such as Cr). On the other hand, the activation energy values of Cr diffusion in Cr-enriched ferritic steels have been reported to be 216 kJ/mol (in Fe-19Cr) and 202 kJ/mol (in Fe-25Cr) [26, 27], which are similar to the activation energy (~212 kJ/mol) found for disappearance of serrations.

Double logarithmic plots of true stress versus strain rate at 573 K for various true plastic strains (ε_{tp}) are shown in Figure 2a. The negative strain rate sensitivity, which is clearly evident from the Regime-2 in the figure, is a manifestation of DSA. At higher strain rates, the true stress increases again, as the effect of DSA diminishes. Figure 2b exhibits the variation of 0.2% offset YS and UTS with temperature. In the temperature range of 573 K to 673 K, there is positive variation of YS and UTS values with temperature, which is also considered a manifestation of DSA [4, 6, 12, 28, 29, 30].

The three distinct regimes observed in Fig. 2a can be explained by corresponding deformation mechanisms [26]. Easy deformation due to free glide and cross slip activity at lower levels of strain rates cause the decrease in true stress in Regime-1 [16]. Regime-2 exhibits abrupt decrease in true stress with strain rate i.e. negative strain rate sensitivity, which is a characteristic manifestation of DSA. Regime-3 shows the increase of true stress with increase in strain rate due to increasing difficulty in easy glide of dislocations. At a particular temperature in the DSA region (573 K), propensity towards occurrence of DSA increases with decrease in true plastic strain. The variation in elongation to fracture and reduction in area with

temperature are shown in Figure 3. Though ductility falls appreciably at the onset of DSA temperature regime, it shows marginal decrease/plateau in the temperature range of DSA. While the variation of elongation to fracture with temperature exhibits a marginal decrease, reduction in area shows a plateau. Unlike most other ferritic steels, the significant appearance of minima in the ductility-temperature variation curve in the DSA temperature range is not observed.

The increase in strength values and decrease in ductility in the temperature range of 573 to 673 K noted for APMT^{TM} steel (Figures 2b and 3) suggest the dominance of DSA. On the other hand, decrease in strength and increase in ductility beyond 673 K exhibits the dominance of recovery processes [31].

5. Conclusions

The APMT^{TM} steel exhibited serrated flow during tensile deformation within a temperature range of 523 K to 673 K at all strain rates. Negative strain rate sensitivity predicts that serrated flow is due to DSA in this temperature range caused by interactions between mobile dislocations and interstitial solutes whose mobility is affected by high concentration of substitutional solutes. Further analysis is needed to fully assess the application of APMT^{TM} steel as a fuel cladding material for the I^{2}S-LWR concept.

Acknowledgment

The research was performed using funds received from the DOE Office of Nuclear Energy's Nuclear Energy University Programs (NEUP). We would also like to acknowledge Professor Bojan Petrovic and Dr. Paolo Ferroni for facilitating the work.

References

1. B. Petrovic, Nucl. Eng. Inter. March (2014) 26-29.
2. B. Jonsson, R. Berglund, J. Magnusson, P. Henning, M. Hattestrund, Materials Science Forum Vol., 461-464 (2004) 455-462.
3. B.K. Choudhary, K.B.S. Rao, S.L. Mannan, Int. J. Pres. Vessels Pip. 58 (1994) 151–160.
4. B.K. Choudhary, K.B.S. Rao, S.L. Mannan, B.P. Kashyap, Mater. Sci. Technol. 15 (1999) 791–97.
5. R.K. Upadhaya, M.N. Shetty, Z. Metallkd. 82 (1991) 19–21.
6. B.K. Choudhary, Mater. Sci. Eng. A 564 (2013) 303–309.
7. D.P. Rao Palaparti, B.K. Choudhary, E.I. Samuel, V.S. Srinivasan, M.D. Mathew, Mater. Sci. Eng. A 538 (2012) 110–117.
8. R. Kishore, R.N. Singh, T.K. Sinha, B.P. Kashyap, Scr. Metall. Mater. 32 (1995) 1297–1300.
9. R. Kishore, R.N. Singh, T.K. Sinha, J. Mater. Sci. 32 (1997) 437–442.
10. S.C. Tjong, S.M. Zhu, Metall. Mater Trans. A. 28A (1997) 1347–1355.
11. C. Keller, M.M. Margulies, Z. Hadjem-Hamouche, I. Guillot, Mater. Sci. Eng. A 527 (2010) 6758–6764.
12. A.K. Roy, P. Kumar, D. Maitra, Mater. Sci. Eng. A 499 (2009) 379–386.
13. S. Kumar, R.P. Kushwaha, B.C. Maji, K. Bhanumurthy, G.K. Dey, Metall. Mater. Trans. A 45A (2014) 531–536.
14. R.L. Klueh, Int. Mater. Rev., 2005, vol. 50, pp. 287–310
15. F. Masuyama, Int. J. Press. Vessels Piping, 2007, vol. 84, pp. 53–61.
16. J. Christopher, B.K. Choudhary, E.I. Samuel, V.S. Srinivasan, M.D. Mathew, Mater. Sci. Eng. A 528 (2011) 6589–6595.
17. W. Karlsen, M. Ivanchenko, U. Ehrnsten, Y. Yagodzinskyy, H. Hanninen, J. Nucl.Mater. 395 (2009) 156–161.
18. M. Ivanchenko, V. Nevdacha, Y. Yagodzinskyy, H. Hanninen, Mater. Sci. Eng. A 442 (2006) 458–461.
19. F. Povolo, E.A. Bisogni, J. Nucl. Mater. 29 (1969) 82–192.
20. A.W. Sleeswyk, Acta Metall. 6 (1958) 598–603.

21. P.G. McCormick, Acta Metall. 20 (1972) 351–354.
22. P. Rodriguez, Bull. Mater. Sci. 6 (1984) 653–63.
23. S.C. Tjong, S.M. Zhu, Metall. Mater Trans. A. 28A (1997) 1347–1355.
24. S.L. Mannan, Bull. Mater. Sci. 16 (1993) 561–582.
25. C.F. Jenkins, G.V. Smith, Trans. Metall. Soc. AIME 245 (1969) 2149-2156.
26. A.W. Bowen, G.M. Leak, Metall. Trans. 1 (1970) 2767-2773.
27. H.W. Paxton, T. Kunitake, Trans. Metall. Soc. AIME 218 (1960) 1003-1009.
28. B.K. Choudhary, K.B.S. Rao, S.L. Mannan, B.P. Kashyap, J. Nucl. Mater. 273 (1999) 315–325.
29. E.I. Samuel, B.K. Choudhary, K.B.S. Rao, Mater. Sci. Technol. 23 (2007) 992–999.
30. B.K. Choudhary, V.S. Srinivasan, M.D. Mathew, Mater. High Temp. 28 (2011)155–161.
31. B.K. Choudhary, E.I. Samuel, G. Sainath, J. Christopher, M.D. Mathew Metall. Mater. Trans. A 44A (2013) 4979–4992.

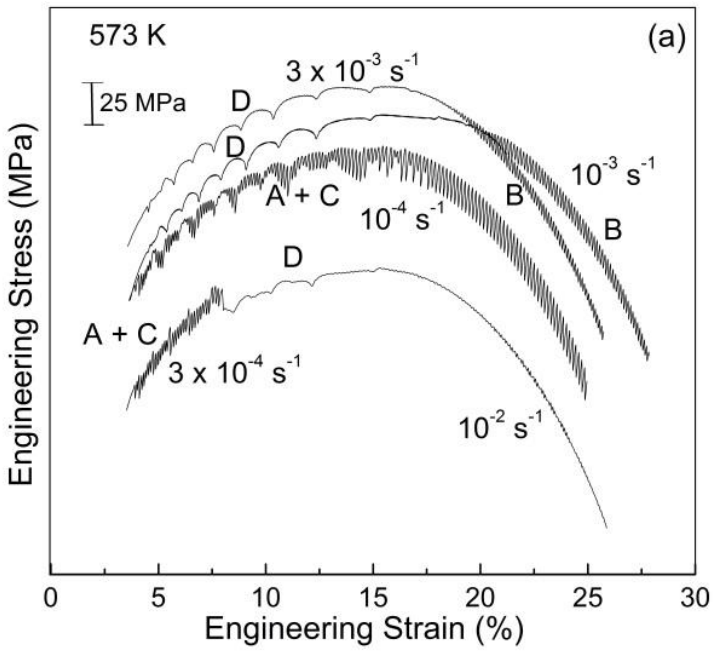

Fig 1(a). Variation of engineering stress with engineering strain at different strain rates at 573 K

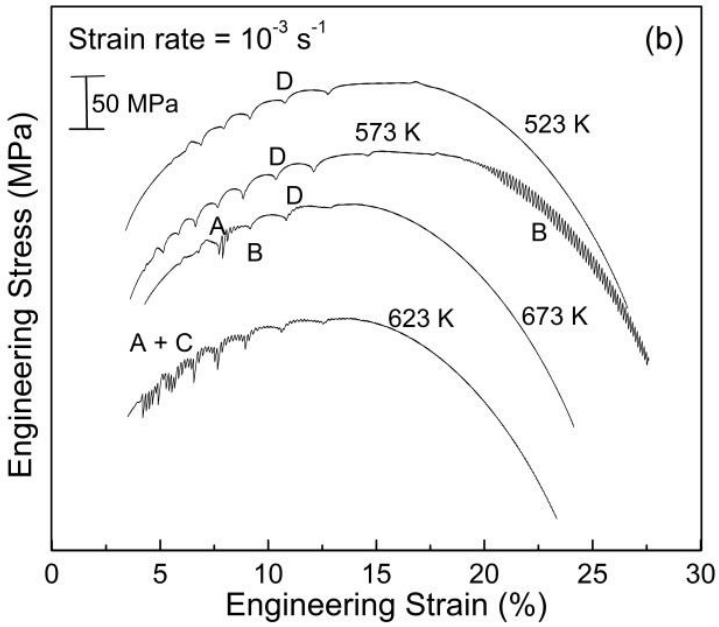

Fig 1(b). Variation of engineering stress with engineering strain at different temperatures at 10^{-3} s^{-1}

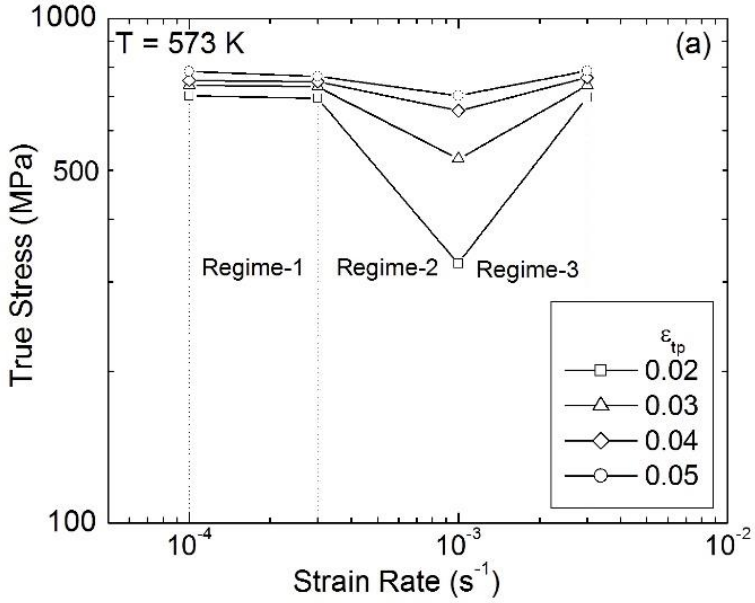

Fig 2(a). Variation of true stress with strain rate at different true plastic strains at 573 K

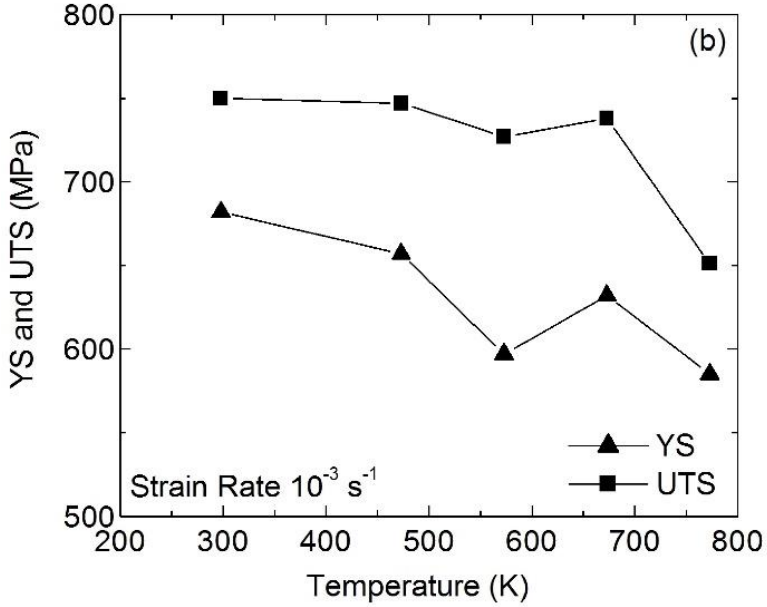

Fig 2(b). Variation of yield stress and ultimate tensile stress with temperature at 10^{-3} s^{-1}

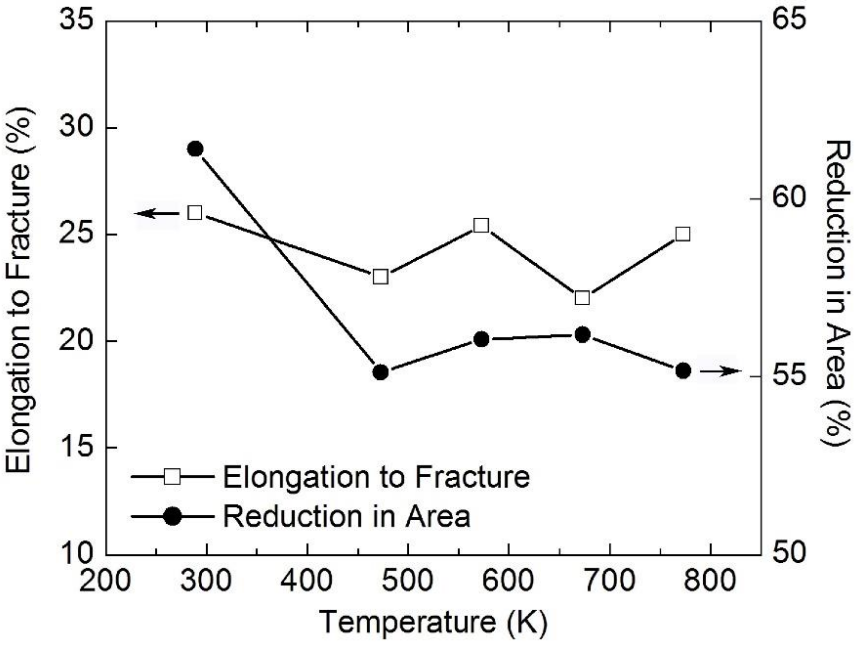

Fig 3. The variation of percentage elongation to fracture and reduction in area as a function of test temperature

Chapter IV
Tensile properties of accident-tolerant aluminum-bearing ferritic steels
"Submitted paper – Annals of Nuclear Energy"

1. Abstract: Tensile behavior of Kanthal APMT^{TM} steel was studied over a temperature range from room temperature to 500 ^{o}C at three strain rates (10^{-4}, 10^{-3} and 10^{-2} s^{-1}). Yield strength, ultimate tensile strength and percentage elongation to fracture were evaluated. Serrated plastic flow was observed in a specific temperature/strain rate regime, signifying occurrence of dynamic strain aging (DSA). Characteristic features of DSA such as plateau/peak in yield and tensile strength as a function of temperature, ductility minima and negative strain rate sensitivity were also observed. The activation energy of serrated flow was found to be affected by diffusion of interstitial impurity modified by high concentration of chromium. Microstructural examination and Vickers hardness testing were also performed on Kanthal APMT^{TM} steel.

Keywords: ferritic steel; accident-tolerant fuel cladding; Kanthal APMT^{TM} steel; tensile test; I^2S-LWR

2. Introduction

Mechanical integrity and enhanced high temperature oxidation/corrosion resistance are some of the main requirements of nuclear fuel cladding materials. Zirconium based alloys are extensively used as nuclear fuel cladding materials in light water reactors (LWR) because of their low neutron capture cross section for thermal neutrons, heat transfer properties, and other favorable characteristics [1]. Nonetheless, the Fukushima-Daiichi incident showed that these alloys are vulnerable to various issues including the risk of explosion due to hydrogen evolution from zirconium-steam reaction under severe accident scenarios such as loss-of-coolant accident (LOCA). Advanced aluminum-bearing, high-chromium ferritic steels such as Kanthal APMT^{TM} have been proposed as possible nuclear fuel cladding material since the aluminum oxide scale provides high oxidation resistance at elevated temperatures [2-4]. APMT^{TM} is an advanced powder metallurgical, dispersion strengthened iron based alloy manufactured by Sandvik Inc. and is generally used as high temperature heating elements up to 1250 ^{o}C under a variety of environments. At elevated temperatures and oxidizing atmospheres, this advanced clad steel develops a dense, non-volatile, thermodynamically stable and adherent oxide (α-Al_2O_3) layer. The combination of excellent oxidation properties and form stability makes the steel unique for high temperature applications [5].

The reported tensile data of APMT steel corresponding to the aforementioned alloy are generally available at temperatures above 800 ^{o}C [6]. During normal operation, the cladding temperature in the I^2S-LWR core is expected to be in the 320-420°C temperature range. Because of the key role played by cladding mechanical properties in fuel rod structural integrity analysis, it is therefore important to obtain mechanical test data of these steels under this

temperature range. In this study, the focus was kept on evaluating tensile properties of APMT^{TM} steel at varying temperatures (room temperature to 500 ^{o}C) and strain rates. This work is expected to lead to the development of correlations between microstructure and mechanical properties of APMT^{TM} steel. This is relevant because of recent studies [1, 4, 7] on this steel mostly focused on the oxidation/corrosion characteristics of this steel, not on its mechanical properties.

3. Materials and Methods

3.1. Material

Two Kanthal APMT^{TM} steel rods of 12 mm diameter and 1830 mm length were procured from Sandvik, Inc. for this study. The rods were received in extruded form and the chemical composition was provided by the manufacturer as Fe-21.5Cr-5.0Al-3.1Mo-0.04C-0.34Si-0.16Mn (in wt.%). Some minor amounts of Y, Zr and Hf are generally found. The APMT^{TM} employs a processing method bit different from the mechanically alloyed powder metallurgy alloys. Instead of mechanical alloying of powder, rapidly solidified powder made by gas atomization is used to produce APMT^{TM} products followed by capsule filling, hot isostatic pressing, machining of billets and hot extrusion [6]. Exact details of the process parameters are not available due to their proprietary nature. For comparison, a Fecralloy steel rod (nominal composition of Fe-22Cr-5Al-0.1Y-0.1Zr along with minor amounts of C, Si, Mn etc. present) of 16 mm diameter was procured from Goodfellow Inc. and tensile tested for this study.

3.2. Microscopic sample preparation

Samples from both longitudinal and transverse cross-sections of a small section of APMT^{TM} steel rod were sectioned and subsequently prepared following standard metallographic procedures. The samples were first hot mounted in Bakelite. After grinding and

polishing, aqua regia (a mixture of hydrochloric acid and nitric acid in 3:1 ratio by volume) was used to perform etching on the metallographic samples to reveal the microstructure. The etched samples were then examined with an Olympus PMG-3 light microscope.

A thin sample disk was sectioned by a diamond saw and mechanically thinned by grinding and polishing to about 50 μm thickness. Next, disks of 3 mm diameter were punched out of the foil using a Gatan mechanical punch. A few disks were electro-jet polished using a Fischione twin jet polisher. The electrolyte used was a mixture of methanol and nitric acid (80:20 ratio by volume) and the voltage used was about 30 V. The jetpolished specimens were examined in a JEOL 2010J transmission electron microscope (TEM) operated at an accelerating voltage of 200kV.

3.3. Mechanical testing

Microhardness tests were performed on the as-polished samples using a Leco LM-100 microhardness tester fitted with a Vickers indenter along two directions (axial and transverse). Tensile specimens of 25.4 mm gauge length and about 6.3 mm gauge diameter were machined keeping the specimen gauge section along the extrusion direction. The specimens were subjected to uniaxial tensile tests in an Instron 5982 tester in the temperature range of 25 to 500 ^{o}C and at nominal strain rates of 10^{-4}, 10^{-3} and 10^{-2} s^{-1}. At first tensile tests were carried out at strain rates of 10^{-4} and 10^{-3} s^{-1} to form a preliminary map of temperature and strain rate combination where serrated flow was observed. Following that, the temperatures for carrying out tensile tests at 10^{-2} s^{-1} were determined. Since our primary objective of this work was to observe mechanical behavior of APMT steel in the temperature range of 320–420 ^{o}C and understand the serrated flow region, further tests were not conducted beyond this range for the

strain rate of 10^{-2} s^{-1}. During each elevated temperature test, the temperature was controlled within ±2 ^{o}C.

4. Results and discussion

4.1 *Microstructural characterization*

Figures 1a and b show optical micrographs of the as-received APMT^{TM} steel specimen along the axial and vertical directions, respectively, as observed by optical microscopy. The microstructures were taken from the center region of the mounted specimen. While the microstructure perpendicular to the axial direction was revealed as equiaxed grains only, the surface in the longitudinal direction exhibited a mixture of some equiaxed grains with mostly elongated grains. Average grain size of the microstructure was found to be 10 ± 2 μm.

Figure 1c shows a TEM image of the APMT alloy (taken from the transverse direction) microstructure of the alloy in detail. The TEM structure reveals much finer grain structure (1 μm) which could not be revealed in the optical micrographs. Furthermore, dislocations were found to be present in these boundaries. That is why it is thought that the grain structure is basically composed by fine subgrains. Electron-back-scatter-diffraction (EBSD) studies are currently being performed, shedding more light on this aspect. The precipitate particles are found to be of two types. The smaller ones (40-65 nm) were found to be present in the (sub)grain interior and the larger particles (100-400 nm) were mostly found to be on the boundaries. Jönsson *et al.* [6] found that the dispersed second phase particles typically consist of oxides, carbides and nitrides, which appear to be resistant to coarsening even after long-term exposure at elevated temperatures.

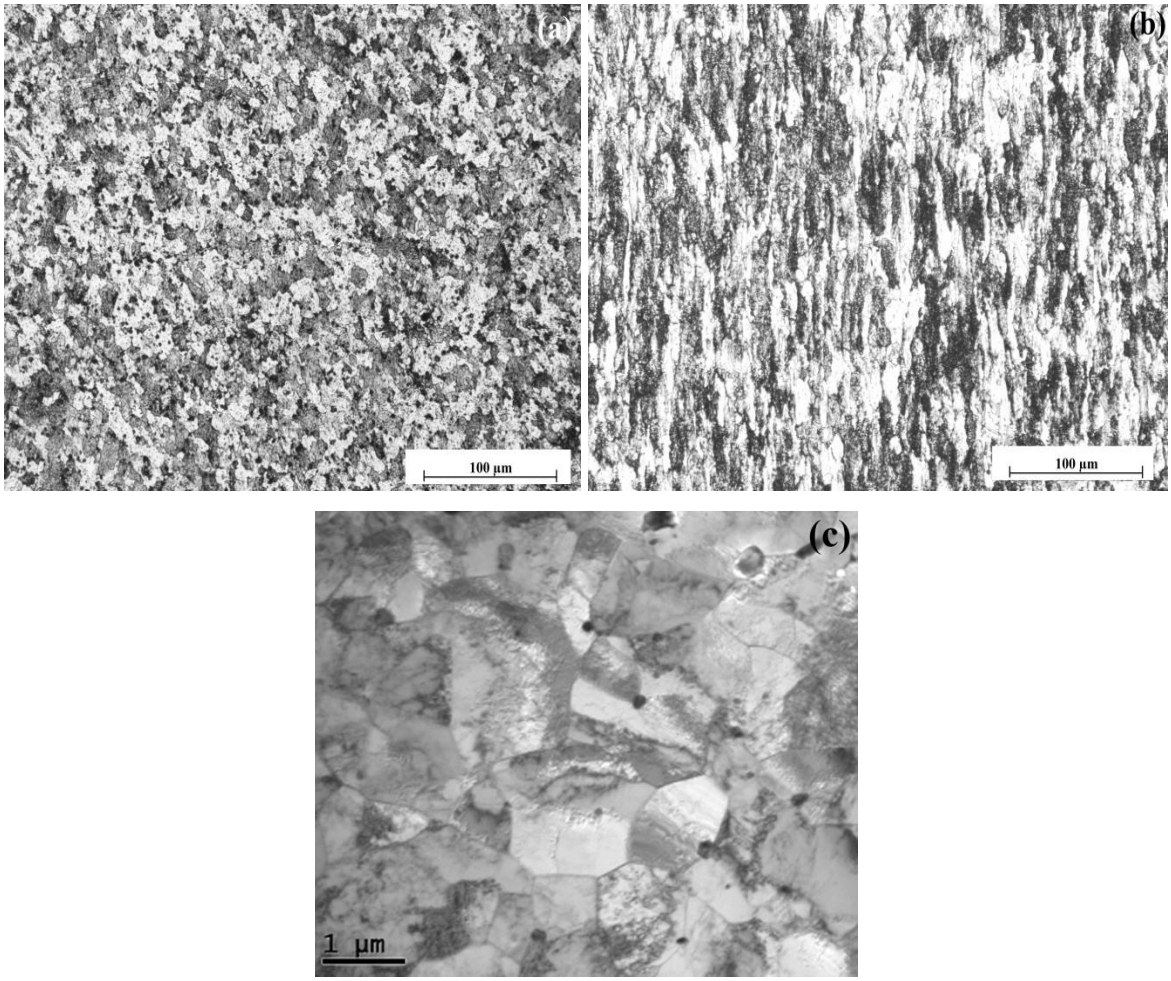

Fig 1. Optical micrographs of APMT^{TM} steel rod surface normal to (a) axial direction and (b) transverse direction. c) A TEM bright field image of the as received APMT^{TM} alloy showing fine (sub) grain structure and second phase particles.

4.2 *Mechanical properties*

Vickers microhardness testing of the APMT rod was performed both along the longitudinal and transverse directions yielding hardness values along the axial direction and vertical to be 307±7 and 316±5, respectively. Thus, it can be concluded that no significant mechanical anisotropy was found to be present between the longitudinal and transverse directions of the extruded rod.

Tensile properties (yield strength, ultimate tensile strength and percentage elongation to fracture), of APMT^{TM} steel tested under different temperatures and strain rates were evaluated. Room temperature tensile properties were evaluated at the strain rate of 10^{-3} s^{-1}. Yield strength was 682 MPa, ultimate tensile strength 750 MPa and elongation to fracture 26%. Figure 2 shows some representative engineering stress-strain curves of APMT^{TM} steel deformed at 10^{-3} s^{-1} at some selected temperatures (25, 300 and 500 ^{o}C). At room temperature, the stress-strain curve was smooth. However, serrations were observed in the temperature range of 250–400 ^{o}C at 10^{-3} s^{-1}. As shown in Figure 2, the stress-strain curve at 300 ^{o}C exhibited distinct serrations. At 500 ^{o}C specimen serrations disappeared on the stress-strain curve at 500 ^{o}C occurred during almost all plastic deformation stage including post-necking deformation regime.

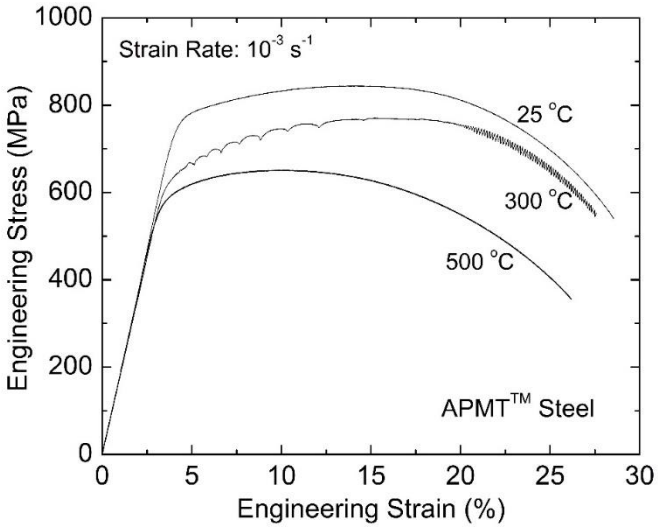

Fig 2. Engineering stress strain curves of APMT^{TM} steel at 10^{-3} s^{-1} for different temperatures

The variations of 0.2% offset yield strength (YS) and ultimate tensile strength (UTS) with temperature for different strain rates (10^{-4}, 10^{-3} and 10^{-2} s^{-1}) are shown in Figures 3a and b, respectively. The plot at 10^{-2} s^{-1} showed a plateau, that at 10^{-3} s^{-1} showed a peak and a plateau, and the curve at 10^{-4} s^{-1} showed a plateau. Figure 3c shows the variation of elongation to fracture

with temperature for different strain rates (10^{-4}, 10^{-3} and 10^{-2} s^{-1}). Ductility variation is not much uniform in this steel. However, there were minima observed in the temperature range of serrated flow at all strain rates. It is important to note that all elongation to fracture values were consistently >20% even in the DSA regime. Tensile tests at higher temperatures were not carried out since the application for this steel does not call for temperatures beyond 420 ^{o}C under normal LWR operating conditions.

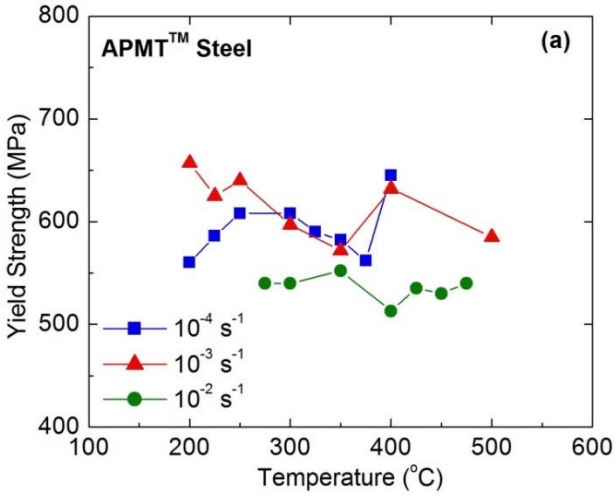

Fig 3(a). The variation of yield strength as a function of temperature of APMT^{TM} steel

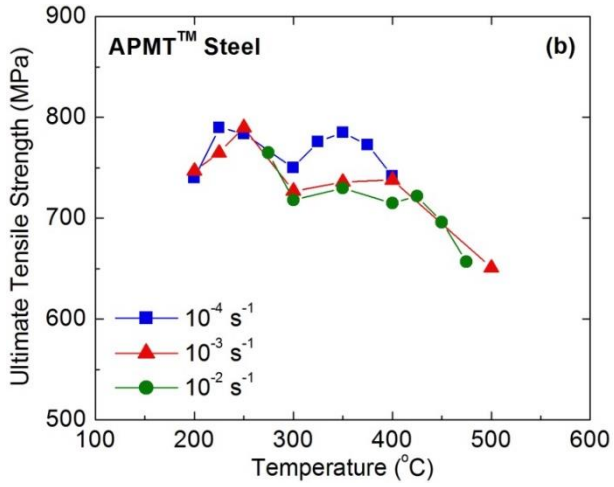

Fig 3(b). The variation of ultimate tensile strength as a function of temperature of APMT^{TM} steel

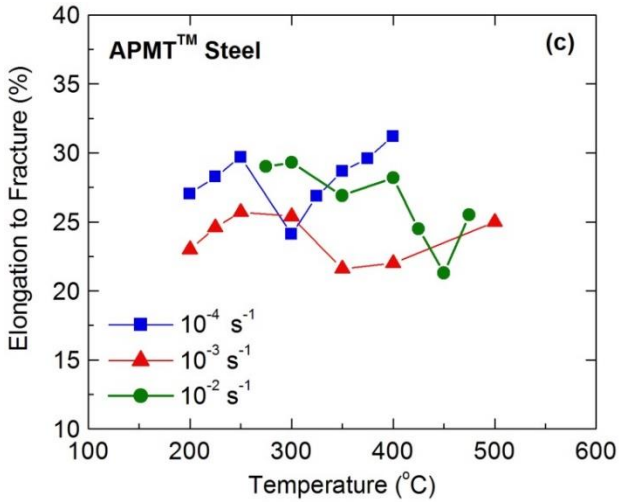

Fig 3(c). Variation of elongation to fracture as a function of temperature of APMT™ steel

Generally, strain rate sensitivity (*m*) is calculated from the following equation:

$$\sigma = C\dot{\varepsilon}^m \qquad (1)$$

where σ is flow stress, $\dot{\varepsilon}$ true strain rate, and *C* a constant. Interestingly, DSA phenomenon is associated with negative strain rate sensitivity. Under normal conditions, the flow stress increases (or decreases) as the strain rate increases (or decreases). That is why *m* values obtained are positive under most conditions. That means resistance to dislocation motion increases as the strain rate is increased and vice versa. However, the opposite is true under DSA. Here the resistance to dislocation movement increases as the strain rate is decreased and vice versa. This is because slower moving dislocations (low strain rate or dislocation velocity) spend longer time in arrest mode at the obstacles, thus providing more time for solutes to diffuse to those dislocations. Solutes develop atmospheres around those dislocation cores and increase flow stress [8]. That is why negative *m* values are obtained. Figure 4 shows *m* values of the APMT™ steel at three temperatures (300, 350 and 400 °C), which coincide with the DSA regime. The flow stress used in the calculation of m was based on the true stress corresponding to yield

stress. The negative *m* values corroborates occurrence of DSA in APMT^{TM}. The fall in ductility in the region of DSA was essentially due to pronounced and rapid drop in necking strain which overplays even the slight increase in strain. The rapid drop in necking strain was due to fall in strain rate sensitivity in the region of DSA [9]. Negative strain rate sensitivity is known to promote flow localization bands which enhances the probability of failure at such sites and thereby reducing the ductility.

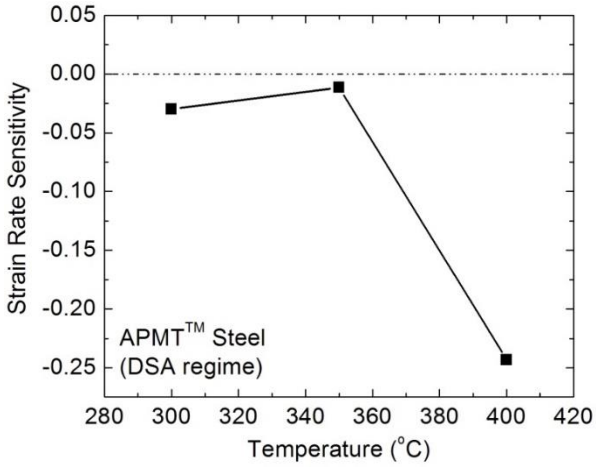

Fig 4. Variation of strain rate sensitivity of APMT steel with temperature under the DSA regime. Note the strain rate sensitivity values are negative.

Figure 5 depicts the strain rate as a function of inverse temperatures for all the elevated temperature tensile tests. The 'filled square' symbol represents tests that exhibited no serrated flow while the 'filled square' symbol represents tests that did show serrated flow. Following the filled symbols, the DSA domain can be configured. One can calculate activation energy for the onset and disappearance of serrated flow (DSA). The activation energy was calculated according to the method proposed by Jenkins and Smith [10]. The activation energy (Q) was determined using the following equation:

$$\dot{\varepsilon} = Aexp\left(-\frac{Q}{RT}\right) \qquad (2)$$

where T is the temperature in K, R is the universal gas constant, A is a constant, and $\dot{\varepsilon}$ has the already defined meaning. The activation energy for the onset of serrations is found to be about 142 kJ/mol whereas for disappearance of the serrated flow is calculated to be about 212 kJ/mol. Decrease in strain rate facilitates larger amount of solutes to diffuse to the dislocations; thus serrations arise at a lower temperature [11]. Both high temperature and low strain rate result in a larger size of solute atmosphere around the dislocations, causing their arrest in the slip path. This explains the typical configuration of Figure 5, where onset and disappearance of serrations occur at lower temperatures with the decrease of strain rates during tensile deformation.

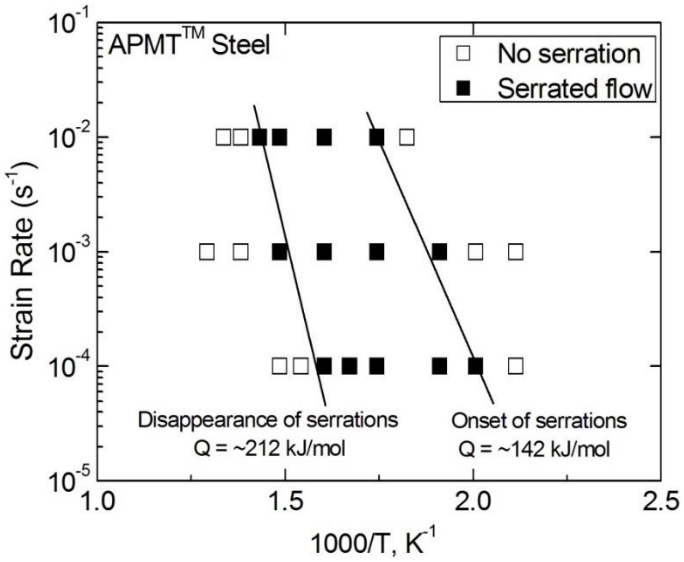

Fig 5. The strain-rate versus inverse temperature plot demarcating the DSA regime with onset of serrations and disappearance of serrations.

Generally, the onset of serrations associated with DSA in low carbon steel and Cr-bearing ferritic-martensitic steels is attributed to interactions between mobile dislocations and carbon and/or nitrogen interstitial impurities, leading to repeated locking and unlocking of dislocations by the interstitial solute atmospheres. To the best of our knowledge, there is no other study which exclusively investigated the DSA effect in Fe-Cr-Al based steels with high

concentration of solutes. Tjong and Zhu [12] investigated the effect of DSA on the creep behavior of a Fe-24Cr-4Al alloy. However, there was no detailed evaluation of deformation kinetics in the serrated flow regime. The present study obtained about 142 kJ/mol activation energy. It is generally accepted that the activation energy values of nitrogen and carbon interstitial atoms in α-Fe are ~76 and ~78 kJ/mol, respectively [13, 14]. Purely interstitial diffusion cannot lead to such high activation energy (142 kJ/mol). Even though the activation energy of carbon diffusion through γ-Fe (FCC) is ~137 kJ/mol [15] being apparently close to 142 kJ/mol, the APMT^{TM} alloy does not contain any austenite. Presence of Cr (21.5%), Al (5%) and Mo (3%), all ferrite-stabilizing elements [16], renders the steel fully ferritic (BCC crystal structure). Thus, carbon diffusion through austenitic phase (FCC) cannot be the mechanism responsible. The most plausible scenario is the modification of the mobility of carbon solutes because of the presence of high concentration of substitutional solutes, especially chromium. However, when the temperature becomes high enough, the importance of interstitial solute atoms becomes less important and gradually shifts to substitutional solute diffusion through the iron lattice leading to the disappearance of serrated flow. In this study, an activation energy of ~212 kJ/mol was obtained for disappearance of serrated flow. This activation energy is found to be lower than the activation energy of lattice self-diffusion in α-Fe or activation energy of chromium diffusion in dilute Fe-Cr alloys, which are quite similar (~250 kJ/mol) [17]. However, some detailed work on chromium diffusion in iron demonstrated that the activation energy of chromium diffusion in iron lattice is gets reduced in concentrated Fe-Cr alloys (such as ~202 kJ/mol Fe-25Cr [18] and ~212 kJ/mol in Fe-19Cr [19]). Thus, the activation energy for disappearance of serrations can be explained. However, this issue needs further in-depth investigation.

4.3. Comparison of APMT™ tensile properties with Fecralloy

Tensile properties of APMT™ alloy are compared with those of Fecralloy rod measured under similar test conditions, as shown in Table 1. At room temperature, the APMT steel has a higher yield strength (by 70.5%) and ultimate tensile strength (by 23.5%) but less elongation to fracture (by 27.7%) compared to Fecralloy. The key to understanding the higher yield strength of APMT™ compared to Fecralloy is through various strengthening mechanisms that may affect the total strength. Four main strengthening mechanisms can be operative in APMT alloy: (1) precipitation strengthening from various type of particles, (2) grain boundary strengthening due to grain refinement (Hall-Petch relationship) and/or subgrain strengthening, (3) solid solution strengthening, and (4) dislocations strengthening [20]. One widely used approach is expressing the yield strength (σ_y) in terms of linear summation of all the strengthening components:

$$\sigma_y = \sigma_o + \sigma_{ss} + \sigma_d + \sigma_b + \sigma_p \qquad (3)$$

where σ_o is the lattice friction stress representing the overall resistance of the crystal lattice to dislocation movement, σ_{ss} is the solid solution strengthening, σ_b is boundary strengthening {either grain size strengthening (σ_{gs}), or subgrain strengthening (σ_s)}, and σ_p is the particle strengthening. Here we can use the concepts of two strengthening mechanisms, solid solution strengthening and sub-grain strengthening to elucidate the difference in the yield strength of APMT™ steel and Fecralloy. APMT™ steel is largely similar in composition with Fecralloy with the exception of molybdenum content (3 wt.%). Each wt.% of Mo in ferrite solid solution may impart about 57.3 MPa [21]. Thus, if all Mo in APMT steel remains in solid solution, it can alone add over 170 MPa to yield strength via the solid solution strengthening mechanism.

Grain size strengthening, also known as the Hall-Petch strengthening, contributes to the yield strength as it varies with grain size (d_g) as shown in the following equation:

$$\sigma_{gs} = k_y d_g^{-0.5}, \quad (4)$$

where k_y is a material-specific constant. On the other hand, substructure strengthening generally varies with subgrain size (d_s)

$$\sigma_s = B d_s^{-1} \quad (5)$$

where B is a constant which depends on microstructural factors.

Furthermore, the presence of fine sub-grains (to the order of 1 μm) would contribute to the APMT yield strength more than what the grain size strengthening (i.e. Hall-Petch strengthening) in Fecralloy would.

Table 1. A comparative list of tensile properties of APMT^{TM} and FeCralloy (all tested at the strain rate of 10^{-3} s^{-1})

Material (Rod)	**Test Temperature** (^oC)	**Yield Strength (MPa)**	**Ultimate Tensile Strength (MPa)**	**Elongation to Fracture (%)**
Kanthal APMT^{TM}	25	682	750	26.0
	300	597	727	25.4
Goodfellow Fecralloy	25	400	583	34.0
	300	251	539	36.0

At 300 ^oC, the yield strength and ultimate tensile strength of APMT steel were about 137% and 34.5% more than those of Fecralloy whereas the elongation to fracture was less by 29.4%. The strengthening mechanisms do get weak at higher temperatures but not in the same way. At this point, no attempt has been made to elucidate those due to lack of fundamental information.

There are many other characteristics of APMT^{TM} steel that are not discussed in this work must be taken into account to assess viability of APMT^{TM} alloy as a fuel cladding material in

the I^2S-LWR design. The effect of thermal aging embrittlement and irradiation performance are some of the issues that need to be addressed. Furthermore, the steel is not produced in the right form needed for use as the fuel cladding material. Under the aegis of the DOE Accident-Tolerant Fuel program, the Oak Ridge National Laboratory has been engaged in developing various compositions of aluminum-bearing ferritic steels [22]. More mechanical properties results from those efforts should become available in the open literature over the upcoming years.

5. Conclusions

APMT^{TM} steel received in the rod form shows quite high yield strength of >500 MPa at all temperatures and strain rates. The ultimate tensile strength was found to be >650 MPa. The trend in ductility was not uniform but remained above 20% (elongation to fracture) under all conditions of testing. Serrations are observed in the stress-strain curves at intermediate temperatures in certain strain rate range due to dynamic strain aging due to solute locking and unlocking of dislocations. The solid solution strengthening imparted by Mo and subgrain strengthening account for the higher yield strength of APMT^{TM} alloy than that of Fecralloy. More detailed analyses are needed to assess APMT^{TM} alloy for I^2S-LWR fuel cladding applications.

Acknowledgments

The research was performed using funds received from the DOE Office of Nuclear Energy's Nuclear Energy University Programs (NEUP). We would also like to acknowledge Professor Bojan Petrovic at Georgia Institute of Technology for leading the I^2S-LWR program and Dr. Paolo Ferroni at Westinghouse for facilitating Materials Working Group's work. We would like

to acknowledge the assistance provided by Drs. T. Williams and S. Pasebani for assistance with the TEM work.

References

1. Murty, K.L., Charit, I., 2008. Structural materials for Gen-IV reactors: Challenges and opportunities. J. Nucl. Mater. 383, 189-195.
2. Zinkle, S.J., Terrani, K.A., Gehin, J.C., Ott, L.J., Snead, L.L., 2014. Accident tolerant fuels for LWRs. J. Nuc. Mater. 448, 374-379.
3. Terrani, K.A., Zinkle, S.J., Snead, L.L., 2014. Advanced oxidation-resistant iron-based alloys for LWR fuel cladding. J. Nucl. Mater. 448, 420-435.
4. Pint, B.A., Terrani, K.A., Brady, M.P., Cheng, T., Keiser, J.R., 2013. High temperature oxidation of fuel cladding candidate materials in steam-hydrogen environments. J. Nucl. Mater. 440 (2013) 420-427.
5. Jönsson, B., Berglund, R., Magnusson, J., Henning, P., Hättestrund, M., 2004. High temperature properties of a new powder metallurgical FeCrAl alloy, Mater. Sci. Forum 461-464, 455-462.
6. Petrovic, B., 2014. The integral inherently safe light water reactor, Nucl. Eng. Inter. March (2014) 26-29.
7. Hellström, K., Israelsson, N., Mortazavi, N., Canovic, S., Halvarsson, M., Svensson, J.-E., Johansson, L.-G. 2015. Oxidation of a dispersion strengthened powder metallurgical FeCrAl alloy in the presence of O_2 at 1100 ^{o}C. Oxid. Met. 83, 533-558.
8. Cunningham S., 1999. Effect of substitutional elements on dynamic strain aging (MS thesis). McGill University, Montreal, Canada.
9. G.E. Dieter, 2001. Mechanical Metallurgy, McGrawHill Publishers, New York.
10. Jenkins, C.F., Smith, G.V., 1969. Serrated plastic flow in austenitic stainless steel. Trans. Metall. Soc. AIME 245, 2149-2156.
11. Rodriguez, P., 1984. Serrated plastic flow. Bull. Mater. Sci. 6, 653–63.
12. Tjong, S.C., Zhu, S.M., 1997. Creep and low-cycle fatigue behavior of ferritic Fe-24Cr-4Al alloy in the dynamic strain aging regime: Effect of aluminum addition. Metall. Mater. Trans. 28A, 1347-1355.
13. Stanley, J., 1949. The diffusion and solubility of carbon in alpha iron. Trans. AIME 185, 752-760.

14. Kucera, J., Stransky, K., 1982. Diffusion in iron, iron solid solution and steels. Mater. Sci. Eng. 52, 1-38.
15. Callister, W.D., Rethwisch, D.G., 2010. Materials Science & Engineering: An Introduction (ed. 8). John Wiley & Sons, USA, 2010.
16. Honeycombe, R.W.K., 1981. Steels: Microstructure and Properties. Edward Arnold, London.
17. Brandes, E.A., Brook, G.B., 1998. Smithells Metals Reference Book, Butterworth-Heinemann, Oxford, UK.
18. Paxton, H.W., Kunitake, H.W., 1960. Diffusion in the Iron-Chromium System. Trans. Metall. Soc. AIME 218, 1003-1009.
19. Bowen, A.W., Leak, G.M., 1970. Diffusion in BCC Iron Base Alloys. Metall. Trans. 1, 2767-2773.
20. Song, R., Ponge, D., Raabe, D., 2005. Improvement in work hardening rate of ultrafine grained steels through second phase particles. Scripta Mater. 52, 1075-1080.
21. Totten, G.E., Xie, L., Funatani, K, Handbook of Mechanical Alloy Design. CRC Press, New York, 2003.
22. Yamamoto, Y., Yang, Y., Field, K.G., Terrani, K., Pint, B.A., Snead, L.L., 2014. Letter Report Documenting Progress of Second Generation ATF FeCrAl Alloy Fabrication.

Chapter V

Comparative Study of Tensile Properties of Accident-Tolerant Aluminum-Bearing Ferritic Alloys

1. Abstract: Aluminum-bearing ferritic steels are being considered as potential accident-tolerant fuel cladding materials for light water reactors (LWR). In this study, various forms of aluminum-rich iron-chromium alloys (APMT^{TM}, APM^{TM}, Fecralloy) are considered for fuel cladding applications in light water reactors (LWR). Tensile tests on all these alloys were performed on all such alloys to systematically compare their mechanical properties as a function of temperature. APMT^{TM} alloy was found to be the most promising material, and thus further characterization focused on this material were done.

2. Introduction: Application of advanced oxidation resistant ferritic alloys as light water reactor fuel cladding is thought to compensate for the limitations of traditionally used Zr based alloy fuel cladding under design based and beyond design based accident scenarios [1,2]. High resistance to irradiation damage, low coefficient of thermal expansion, high thermal conductivity, combination of chromium and aluminum providing resistance to attack against steam, good mechanical properties at temperatures even above the operating temperature, less expensive primarily due to absence of nickel and good resistance to environmental cracking put this alloy in the forefront of all materials under consideration for fuel cladding [3]. To minimize penalties in cycle length due to high neutron absorption in the iron based alloys with modest impact on the economics, a combination of cladding thickness reduction and fuel enrichment increase (~0.5%) has been proposed.

Tensile, creep, and low cycle fatigue properties are few of the important considerations for the design of nuclear reactor components operating at high temperatures. Evaluation of

elevated temperature tensile properties is a preliminary step toward characterization of the materials' performance for nuclear fuel cladding applications. In view of this, investigation of tensile properties of APMT^{TM} rod, APMT^{TM} tube, APM^{TM} tube and Goodfellow Fecralloy rod was done. The mechanical properties of these alloys were compared with those of a 2nd generation nuclear grade ATF alloy, C35MN and the traditionally used Zircaloy-4.

APMT^{TM}, being a promising material among the ones under our current study, further characterization was done on the alloy

3. Experimental details and analysis of data:

A. Material: Kanthal APMT^{TM} rods (Fe-21.45Cr-4.94Al-3.09Mo-0.039C-0.34Si-0.16Mn-0.008P, wt. %) of 12 mm diameter, Kanthal APMT^{TM} tubes of same composition as APMT^{TM} rods, 26.7 mm outer diameter and 2.8 mm wall thickness and Kanthal APM^{TM} tube (Fe-21.5Cr-5.7Al-0.031C-0.33Si-0.2Mn, wt.%) were procured from Sandvik Inc. for this study. The materials were received in extruded form and the chemical composition was provided by the manufacturer. Some minor amounts of Y, Zr and Hf are generally found. The APMT^{TM} and APMT^{TM} employs a processing method bit different from the mechanically alloyed powder metallurgy alloys. Instead of mechanical alloying of powder, rapidly solidified powder made by gas atomization is used to produce the products followed by capsule filling, hot isostatic pressing, machining of billets and hot extrusion [4]. Exact details of the process parameters are not available due to their proprietary nature. For comparison, a Fecralloy steel rod (nominal composition of Fe-22Cr-5Al-0.1Y-0.1Zr along with minor amounts of C, Si, Mn etc. present) of 16 mm diameter manufactured by Goodfellow Inc. and Zircaloy-4 rod (Zr-1.5Sn-0.2Fe-0.1Cr, wt. %) were also procured for the present study.

B. Tensile Testing and Analysis of Data: Tensile specimens of 25.4 mm gauge length and about 6.3 mm gauge diameter were machined from the rods keeping the specimen gauge section along the extrusion direction. Tubes were machined into curved specimens of gauge length 29 mm, thickness 2.8 mm and width 5 mm. The specimens were subjected to uniaxial tensile tests in an Instron 5982 tester in the temperature range of 25 to 500 ^{o}C and a nominal strain rate of 10^{-3} s^{-1}. During each elevated temperature test, the temperature was controlled within ±2 ^{o}C. The yield stress (YS), ultimate tensile stress (UTS) and elongation to fracture obtained from the tensile curves of our tests were compared with that of extruded C35MN (13Cr-4.5Al-2Mo-1Nb-0.15Y-0.2Si, wt. %) alloy [5]. Extensive study on APMT was carried out following this comparison.

C. Optical microscopy, Fractography, Transmission Electron Microscopy and Electron Backscatter Diffraction of APMT^{TM}: Since, APMT^{TM} was found to be a promising material in the current study, more characterization was done on it. A sample from APMT^{TM} was sectioned and subsequently prepared following standard metallographic procedures. The sample was first hot mounted in Bakelite. After grinding and polishing, glycergia (a mixture of hydrochloric acid, glycerol and nitric acid in 3:2:1 ratio by volume) was used to perform etching on the metallographic samples to reveal the microstructure. The etched sample was then examined with an Olympus PMG-3 light microscope. To understand the phases present in the microstructure, X-Ray diffraction (XRD) was done on the as received sample to understand the possible phases present in it.

Fracture surfaces were examined under a field emission scanning electron microscopy (SEM) to understand the nature of fracture and evolution of fracture surface features with temperature. The SEMs were done at an accelerating voltage of 20 kV. To understand the dislocation substructure or nature of particles as well as strengthening mechanisms in region of

serrated flow, transmission electron microscopy (TEM) was done on an as-received sample and the sample tensile tested at 300 ^{o}C and 10^{-3} s^{-1}. For TEM, thin sample disks were sectioned from the samples by a diamond saw and mechanically thinned by grinding and polishing to about 50 μm thickness. Next, disks of 3 mm diameter were punched out of the foil using a Gatan mechanical punch. A few disks were electro-jet polished using a Fischione twin jet polisher. The electrolyte used was a mixture of methanol and nitric acid (80:20 ratio by volume) and the voltage used was about 30 V. The jet-polished specimens were examined in a JEOL 2010J TEM operated at an accelerating voltage of 200kV. Energy dispersive spectroscopy (EDS) was done on the particles present in the TEM micrographs to get an idea of the elements playing a pivotal role in the serrated flow showed by the steel during tensile testing. To study the microstructure in detail and strengthening mechanisms causing serrated flow in APMT^{TM}, electron backscattered diffraction (EBSD) was done on the as-received and the sample tensile tested at 300 ^{o}C and 10^{-3} s^{-1}. For EBSD, the sample was polished in a vibratory polisher for 4 hours. EBSD was done using a JSM-6610 LV JEOL SEM fitted with a backscatter detector and analyses were done using the TSL-OIM software.

4. Results and discussion

A. Results from tensile tests: Figure 1a shows the variation of yield stress (YS) with temperature for all the materials under study. APMT^{TM} rod shows the highest YS at all temperatures. The YS of extruded C35MN is ~20% less in the temperature range of 200-500 ^{o}C. At all elevated temperatures, the YS of APMT rod is ~130% more than that of Fecralloy.

Among the tubes, APMT^{TM} has a much higher YS than APM^{TM} at room temperature. Though the difference in strength values decreases at higher temperatures and becomes almost equal at 300 ^{o}C, APMT^{TM} tube shows higher YS that APMT^{TM} at all other temperatures. The rod

samples exhibit more YS than tube samples. Figure 1b exhibits the variation of ultimate tensile stress (UTS) with temperature for the materials. At room temperature, C35MN shows higher UTS than APMT, but at higher temperatures, the UTS of both the materials are close. At 300 ^{o}C, the UTS of APMT^{TM} and C35MN are higher than that of Fecralloy by 34.5%.

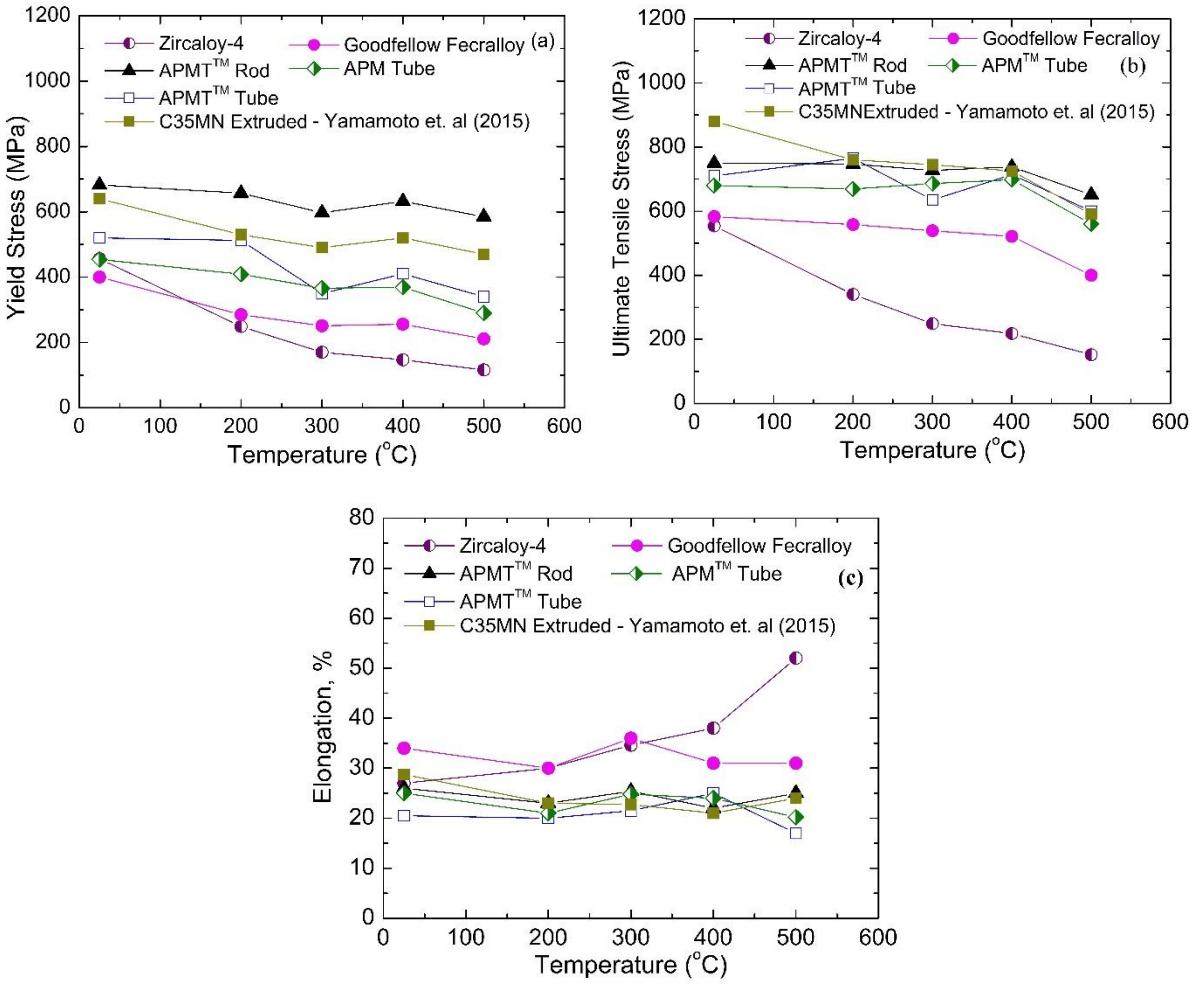

Figure 1: Variation of (a) YS with temperature (b) UTS with temperature and (c) Elongation to fracture with temperature of APMT^{TM} rod

Zircaloy-4 shows much lesser (>100%) UTS than APMT. Figure 1c shows the variation of elongation to fracture with temperature of the materials under current study. Elongation to fracture of Zircaloy-4 increases with rise in temperature. But the elongation to fracture of the

Fe-Cr-Al alloys are less than that of Zircaloy at high temperatures. But, at all temperatures, their ductility remains above 20%.

A. Results from Optical microscopy, Fractography, Transmission Electron Microscopy and Electron Backscatter Diffraction of APMT^{TM}: Figures 2a and 2c show the microstructure of an as-received APMT alloy in axial and longitudinal directions, respectively. The micrograph from the axial section of APMT rod shows polygonal equiaxed grains of average diameter of 10 μm and that from longitudinal section revealed elongated grains in the extrusion direction with a grain size of about 40 μm. X-ray diffraction was done on the as-received APMT rod sample to detect the presence of precipitates in the sample. It was found that there are Fe-Cr, Al-Cr-Fe and small amount of Cr-Mo-Fe precipitates in the matrix of the sample. However, recent researched have predicted the present of other phases like laves phases and $M_{23}C_6$ particles.

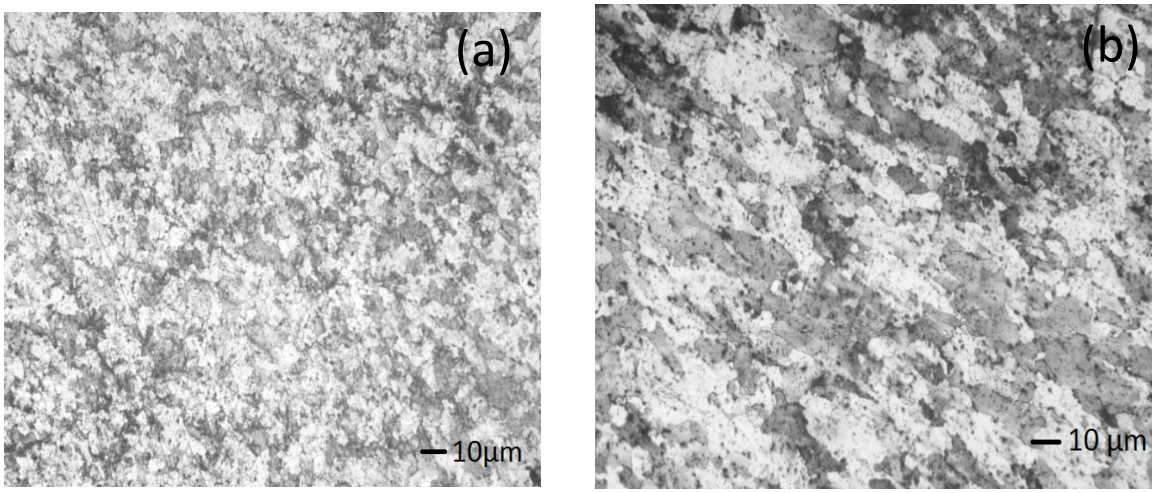

Figure 2: Optical microscopy of APMT^{TM} rod at 100× in (a) normal to axis direction and (b) longitudinal direction

Figure 3 depicts the microstructures of deformed APMT samples. Figure 3(a), 3(c) and 3(e) reveal the microstructures on the fracture surface of Kanthal APMT alloy rod sample deformed at room temperature, 300 ^{o}C and 500 ^{o}C respectively. Figures 3(b), 3(d) and 3(f) show

the micrographs of the transverse section of the deformed (necked) portion of the specimens deformed at room temperature, 300 ºC and 500 ºC respectively. The microstructures of the transverse section show prominent elongated grains.

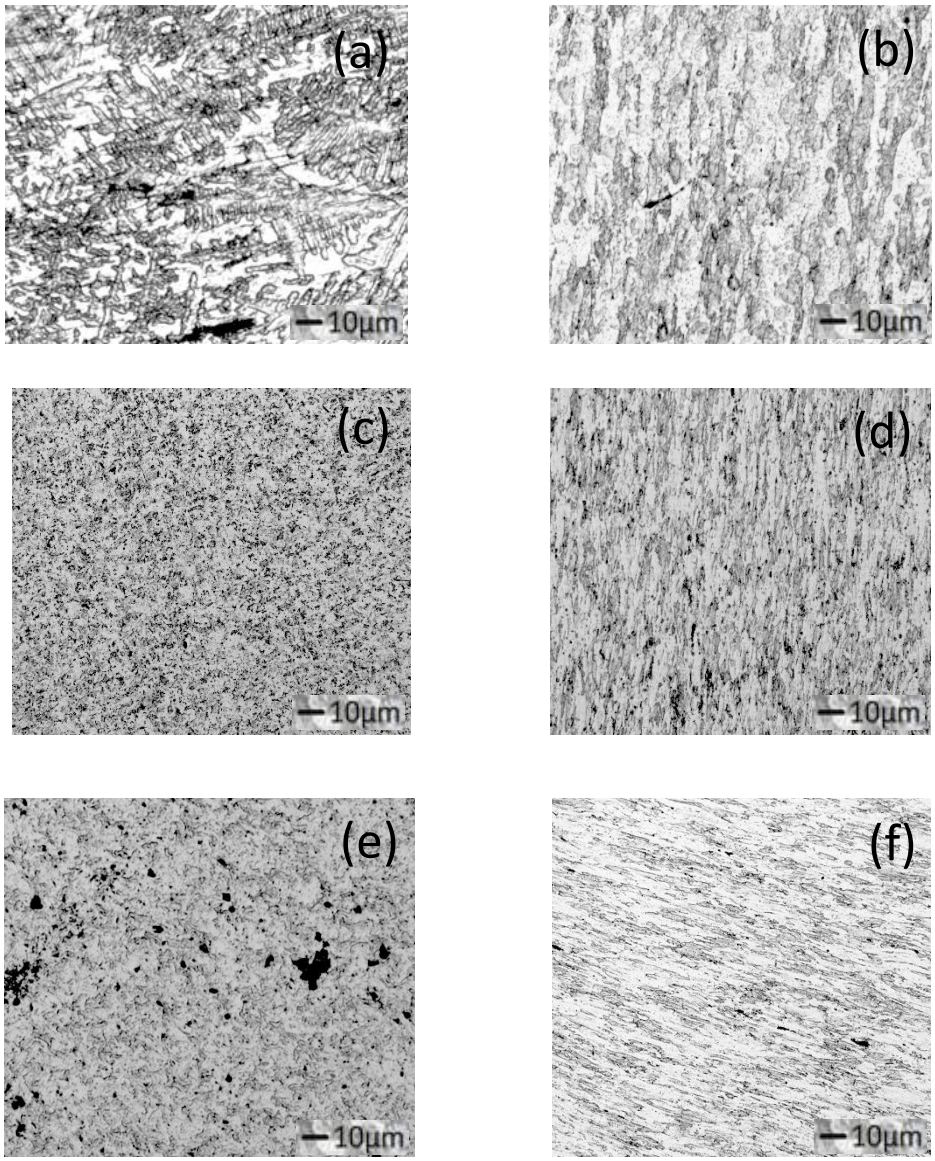

Figure 3: Optical micrographs at a magnification of 100× of Kanthal APMT rods deformed at a strain rate of 10^{-3} s^{-1}: on fracture surface (a) at 25 ºC, (c) at 300 ºC, (e) at 500 ºC, and in transverse direction (b) at 25 ºC, (d) at 300 ºC, and (f) at 500 ºC

Figure 4 shows the fracture surfaces of tensile tested APMT steels at different temperatures at a strain rate of 10^{-3} s^{-1}. At room temperature, chisel tip appearance along with

ductile dimples can be seen in Figure 4(a) and 4(b). With increase in temperature, significant reduction in the regions having chisel tip appearance is observed and the fracture was dominated mainly by the presence of equiaxed dimples (Figure 4(c) and 4(d)). The size of equiaxed dimples increases with increase in temperature, indicating decrease in the number of microvoid nucleation and dominance of growth process at high temperatures. The observed transgranular fracture mode following tensile deformation of APMT at intermediate temperatures is in agreement with those reported for other ferritic steels. Presence of transgranular fracture rules out intergranular cracking as the possible reason for the reduction in strength values at high temperatures in Kanthal APMT steel.

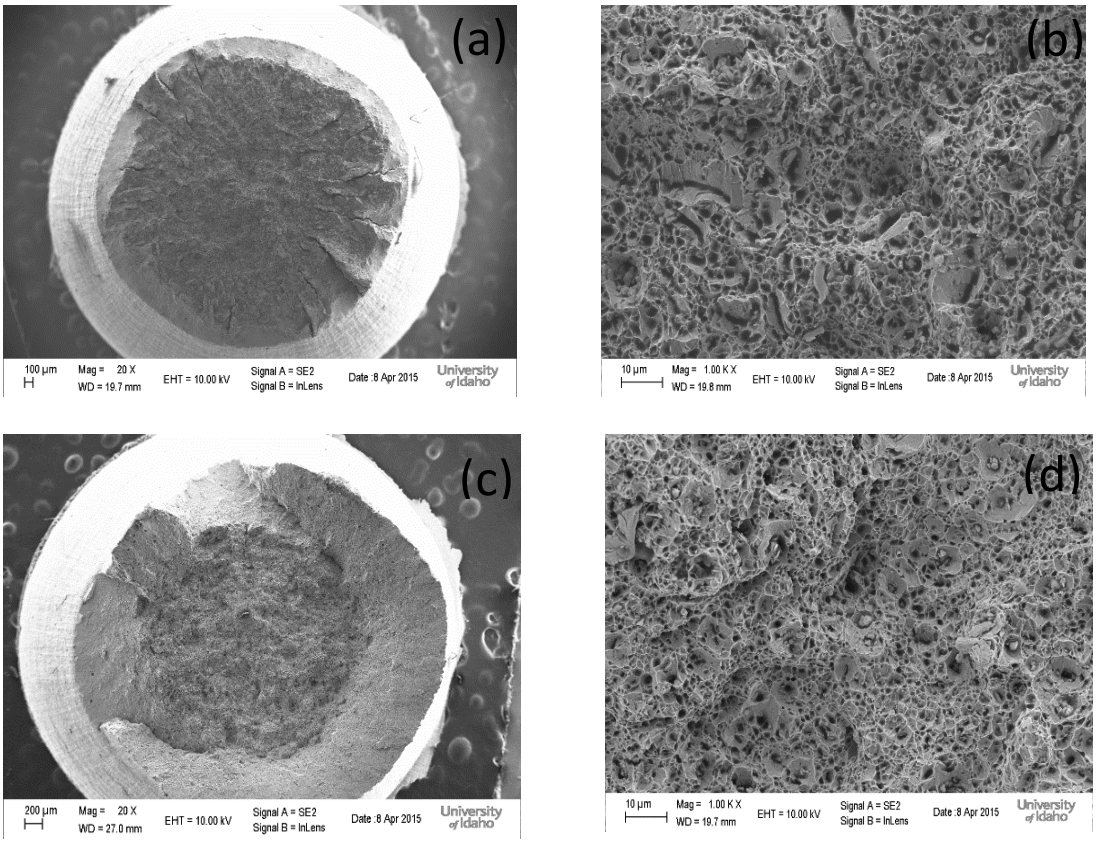

Figure 4: Fractography of APMT^{TM} rod tensile tested at 10^{-3} s^{-1} (a) at room temperature at 20×, (b) at room temperature at 1000×, (c) at 300 ^{o}C at 20× and (d) at 300 ^{o}C at 1000×

To observe if there was any difference between the fractography of samples deformed at different strain rates, fractography of samples deformed at 300 ^{o}C and 10^{-4} s^{-1} and 10^{-2} s^{-1} were performed. Figures 5a and b show the fracture surfaces of deformed APMT rod samples at 300 ^{o}C at strain rates of 10^{-4} and 10^{-2} s^{-1}, respectively.

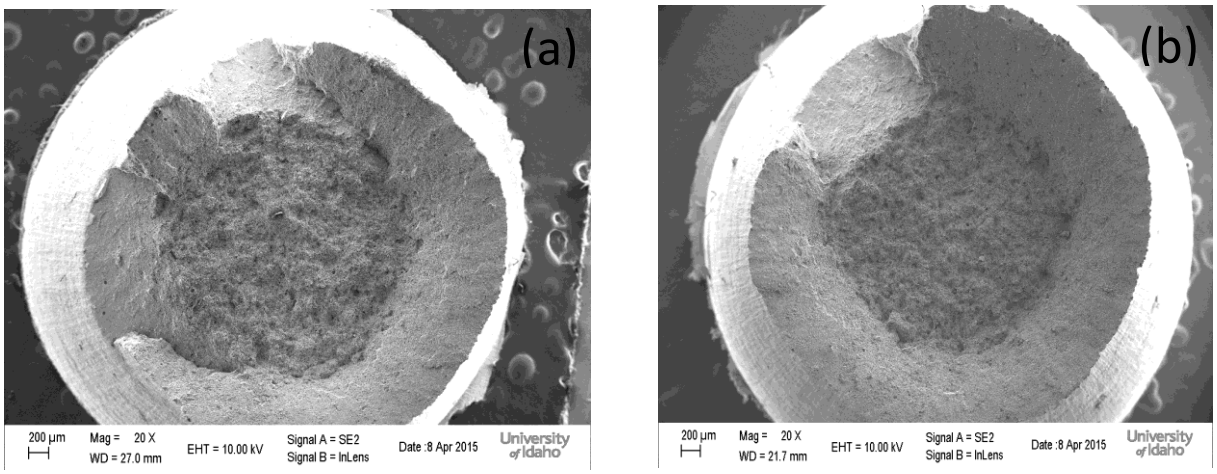

Figure 5: Fractography of APMT^{TM} rod tensile tested at room temperature at (a) 10^{-4} s^{-1} and (b) 10^{-2} s^{-1}

Transmission electron microscopy (TEM) was done on APMT as received samples. Figures 6 (a-c) show the TEM images of as received APMT rod samples before subjected to deformation. The micrographs show subgrains and low dislocation density. Small particles of 40-65 nm were present in the subgrains and large particles of 100-400 nm were observed along the grain boundaries. Figures 6 (d-f) exhibit the TEM images of deformed APMT rods tensile tested at 300 ^{o}C and 10^{-3} s^{-1}. Dislocation substructure was observed with particles obstructing their motion. EDS was carried out on the particles and they were found to be aluminum-rich particles as shown in Figure 7. However the matrix was Fe and Cr rich.

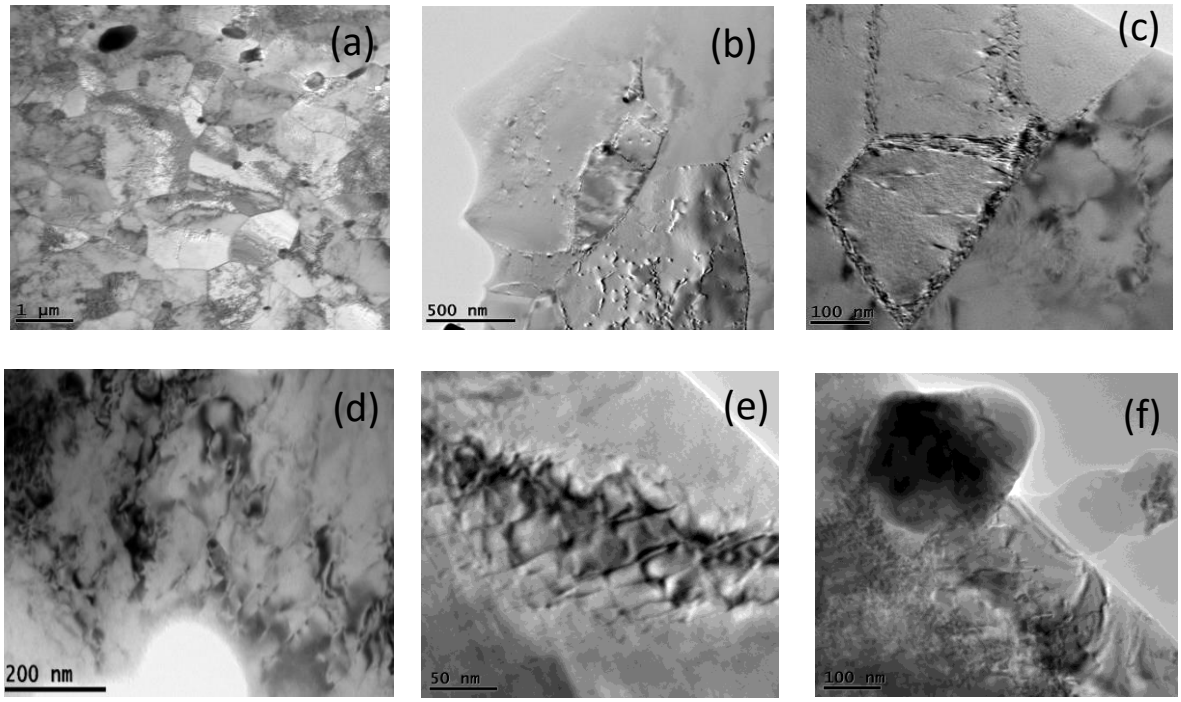

Figure 6: (a-c) TEM images of as-received Kanthal APMT rods; (d-f) APMT Kanthal rod tensile deformed at 300 ^{o}C at 10^{-3} s^{-1}

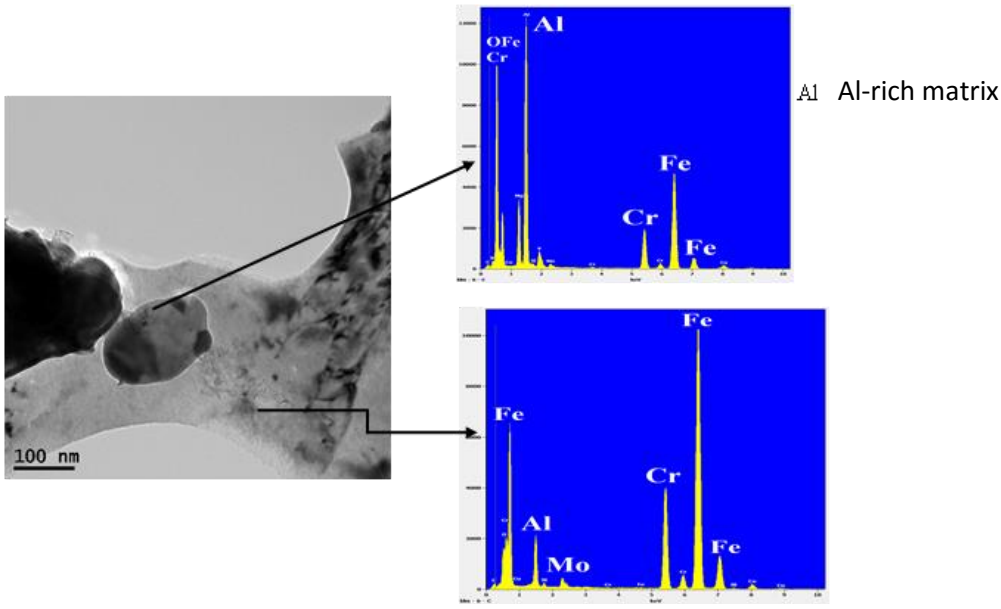

Figure 7 showing a particle in a deformed APMT sample and the EDS characterization on it and the matrix around it

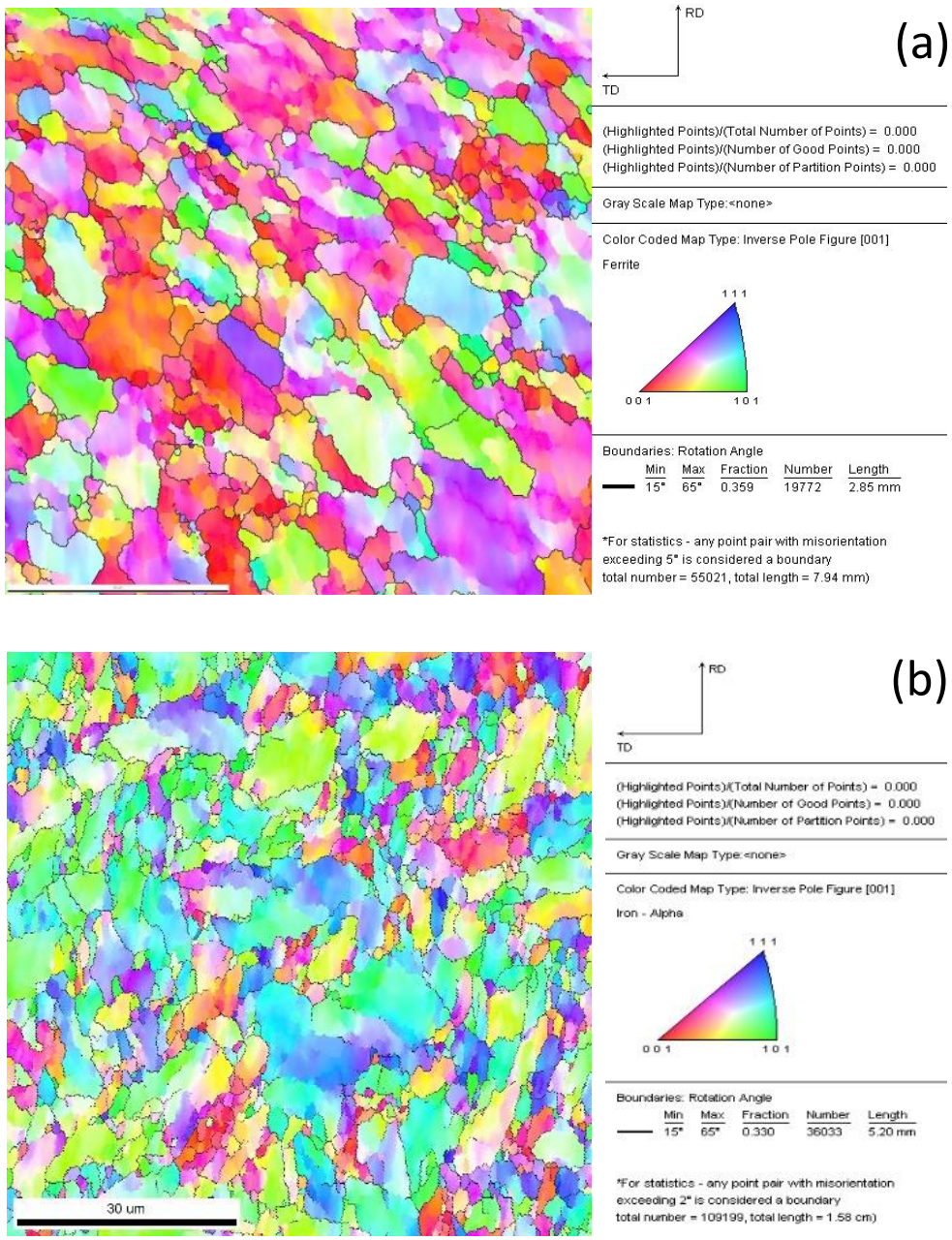

Figure 8: Inverse pole figure maps of APMT rod (a) in as-received condition and (b) deformed at 300 ^{o}C at 10^{-3} s^{-1}

EBSD was done on the as-received and tensile deformed sample in the serrated flow region to understand more about the microstructure and strengthening mechanisms. Figure 8a and 8b show the inverse pole figure (IPF) map of as received and tensile deformed APMT^{TM} sample at 300^{o}C, respectively. IPF maps show the presence of subgrains in the microstructure.

Partitioning was done on the basis of low (0 – 15º) and high (15º – 65º) angle in both IPF maps. It was found that 36% of the grain boundaries are high angle and remaining 64% low angle in the as-received sample. After tensile testing at 300 ºC, there was 58% of high angle grain boundaries and the remaining low angle. This observation appears to imply that subgrain structure disintegrates to quite an extent forming high angle grain boundaries.

5. Conclusions: APMT^{TM} is a potential material for fuel cladding on the basis of strength and ductility at intermediate temperatures in unirradiated condition. TEM shows prominent presence of subgrains in the as-received sample. The sample deformed at 300 ºC at 10^{-3} s^{-1} shows presence of dislocation substructure and particles entangled in them. Also EBSD shows presence of subgrains. Thus, the high strength of APMT can be largely contributed to the presence of subgrains leading to subgrain strengthening.

References:

1. Zinkle, S.J., Terrani, K.A., Gehin, J.C., Ott, L.J., Snead, L.L., Accident tolerant fuels for LWRs. J. Nuc. Mater. 448 (2014), 374-379.
2. Terrani, K.A., Zinkle, S.J., Snead, L.L., Advanced oxidation-resistant iron-based alloys for LWR fuel cladding. J. Nucl. Mater. 448 (2014), 420-435.
3. Raul B. Rebak, 2015. Alloy selection for accident tolerant fuel cladding in commercial light water reactors, Met. and Mater. Trans E., Vol. 2 (2015), 197-207
4. Petrovic, B., The integral inherently safe light water reactor, Nucl. Eng. Inter. March (2014) 26-29
5. Y. Yamamoto, B.A. Pint, K.A. Terrani, K.G. Field, Y. Yang, L.L. Snead, "Development and Property Evaluation of Nuclear Grade Wrought FeCrAl Fuel Cladding for Light Water Reactors," J.Nucl. Mater., submitted, (2015)

Appendix I

Tensile Deformation Behavior of Al-rich Ferritic Steels for Advanced Light Water Reactors

"Submitted paper for publication in the proceedings of International Conference on Frontiers in Materials Processing, Applications, Research and Technology"

Ankan Guria, Indrajit Charit and Bojan Petrovic
icharit@uidaho.edu

1. Abstract: Following the Fukushima-Daiichi incident, there has been considerable interest in developing accident-tolerant fuel cladding materials to make light water reactors (LWRs) more resistant to such accidents. Traditionally, zirconium-based alloys are used as the fuel cladding material in these reactors. Exothermic reaction with steam under accident conditions may lead to production of hydrogen with the possibility of catastrophic consequences. Hence, aluminum-rich (around 5 wt.%) ferritic steels such as Fecralloy, APMT^{TM} and APM^{TM} have potential for accident-tolerant fuel cladding applications. These materials create an aluminum-based oxide scale protecting the alloy at elevated temperatures. Tensile deformation behavior of Fecralloy and APMT^{TM} alloy were compared at different temperatures (25-500 ^{o}C) and strain rates, and correlated with microstructural characteristics. Serrations appeared in the stress-strain curves of these alloys tested in a limited temperature range (300-400 ^{o}C). Presence of serrations did not lead to a decrease in elongation to fracture despite showing negative strain rate sensitivity behavior. The appearance of serrations is explained on the basis of dynamic strain aging (DSA) effect due to solute-dislocation interactions. Hence, a fuel/cladding system containing Fe-Cr-Al steel cladding can be viable for a novel Integral Inherently Safe LWR (I^2S-LWR) concept currently under development.

Keywords: Light water reactors, steel, Fecralloy, APMT^{TM}, serrations, dynamic strain aging

2. Introduction: Zirconium based alloys have been extensively used as nuclear fuel cladding materials in light water reactors (LWRs) because of low thermal neutron capture cross-section, good heat transfer properties, adequate mechanical properties and many other favorable characteristics [1]. However, there are other concerns with zirconium based alloys including severe oxidation at elevated temperatures leading to extensive hydrogen evolution due to exothermic zirconium-steam reactions during accident situations such as loss-of-coolant accident (LOCA) [2]. In theory, aluminum-bearing ferritic steels (such as Fecralloy, Kanthal APMT^{TM} etc.) may be used as an alternative class of materials with the potential for nuclear fuel cladding applications in LWRs mainly due to their superior high temperature oxidation/corrosion resistance under extreme conditions despite neutronic penalties [2-5]. These steels have Fe-22Cr based compositions with significant aluminum content (about 5 wt.%). Notably, APMT steel contains about 3 wt.% Mo imparting high elevated temperature strength [6]. At elevated temperatures and other oxidizing atmospheres, these steels develop a thin, dense, inert, non-volatile, thermodynamically stable and adherent oxide (α-Al_2O_3) layer [3, 6]. The combination of excellent oxidation properties and form stability makes these steels unique. In an ongoing research project, a Georgia Tech led team is working on developing a conceptual design of an Integral Inherently Safe Light Water Reactor (I^2S-LWR) in which aluminum-containing ferritic steel such as APMT^{TM} is being considered as a potential alternative to zirconium based fuel cladding material [5].

The present work has been focused on evaluating tensile properties of Fecralloy under varied temperature and strain rate conditions. Tensile results obtained from APMT^{TM} are also compared with those from Fecralloy. The high temperature oxidation and corrosion resistance of these aluminum-bearing steels have been extensively studied. However, there is no reported

work comparing the tensile properties of Fecralloy and APMT^{TM} in the temperature range of 25-500 ^{o}C. This temperature range is pertinent for the normal operating temperature regime of the advanced light water reactor. Apart from the tensile behavior, an attempt was also made to shed light on structure-property correlations by evaluating microstructural characteristics by optical microscopy and transmission electron microscopy.

3. Materials and experimental procedure: A Fecralloy steel rod of 16 mm diameter was procured from Goodfellow Inc. for this study. For comparison, Kanthal APMT^{TM} alloy rod of 12 mm diameter was also procured from Sandvik Inc. While the Fecralloy has a nominal composition of Fe-22Cr-5Al-0.1Y-0.1Zr along with other minor elements (composition close to Kanthal APM^{TM}), Kanthal APMT^{TM} is an advanced powder metallurgical, dispersion strengthened iron based alloy (Fe-21.5Cr-5.0Al-3.1Mo-0.04C-0.34Si-0.16Mn, wt.%).

Optical metallographic samples were prepared using standard metallographic procedures. After grinding and polishing down to 1 μm surface finish, metallographic samples were etched by a mixture of hydrochloric acid and nitric acid (3:1 by volume). Microstructural characterization of as-received Fecralloy rod was carried out using optical microscopy (OM). Vickers microhardness tests were performed on the as-polished samples using a LECO 100M microhardness tester by applying a load of 0.5 kg-f (4.91 N) for 15 s.

Round tensile specimens of 25.4 mm gauge length and around 6 mm gauge diameter were machined from the rods. They were subjected to uniaxial tensile tests with an Instron machine in the temperature range of 25 to 500 ^{o}C using a nominal strain rate 10^{-3} s^{-1}. Selective tensile tests using other strain rates such as 10^{-4} s^{-1} and 3×10^{-3} s^{-1} were also performed. The temperature in all the tests was controlled within ±2 ^{o}C. The 0.2% offset yield strength (YS), ultimate tensile

strength (UTS) and elongation to fracture (E_f) were measured. Fractographic examinations were carried out on the tested specimens using the secondary electron (SE) imaging mode in a Zeiss Supra-35 scanning electron microscope (SEM) operated at an accelerating voltage of 20 kV. Transmission electron microscopy of the steels was carried out to obtain microstructural characteristics using a JEOL 2010J transmission electron microscope (TEM) operated at 200 kV. The TEM sample preparation was done by Fischione twin electro-jetpolisher using an electrolyte mixture of methanol and nitric acid (80:20 by volume).

4. Results and discussion

4.1. Microstructural characteristics: Figure 1a shows the microstructure of the as-received Fecralloy steel specimen as observed by optical microscopy. The microstructure was taken from the center region of the mounted specimens. The microstructure was composed of equiaxed grains. However, there was a slight variation in the grain size among the different sections. The average grain size was measured to be about 25 μm using the mean linear intercept technique. On the other hand, APMT^{TM} grain structure as shown in Figure 1b was much finer (about 10 μm). Figure 2 shows TEM images of the as received Fecralloy rod. The dislocation density and particle density were found to be low. Some fine second phase particles (diameter of 21±7 nm) were present as evidenced in Figure 2a. However, as shown in Figure 2b there were also some larger particles with varying sizes from 500 nm to 1 μm found mostly along grain boundaries. The density of these larger particles was not that high and they were localized only at certain regions. Figure 3 shows a TEM image of the APMT alloy microstructure in detail. The TEM micrograph revealed a much finer (sub) grain structure (1-3 μm) which could not be resolved properly by optical microscopy. Further examination revealed presence of dislocations

in these boundaries while dislocation density in grain interiors was minimal. That is why it is thought that the microstructure is basically composed of fine subgrains contained in the larger grain structure. Precipitate particles are found to be of two types. The smaller particles (40-65 nm) were found to be present in the (sub) grain interior and larger particles (100-400 nm) were mostly detected on the boundaries.

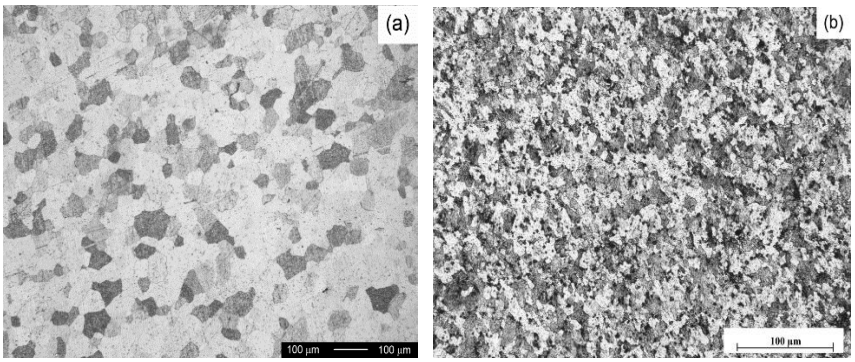

Figure 1. Optical micrographs of (a) Fecralloy rod and (b) APMT rod in the transverse section.

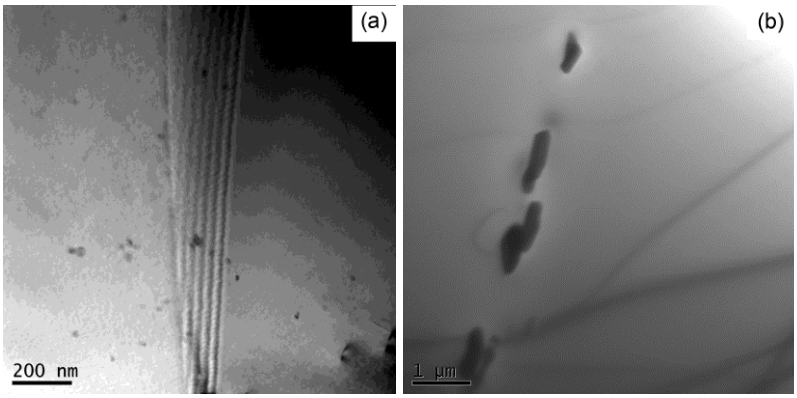

Figure 2. Transmission electron microscopy images of Fecralloy showing (a) fine particles and (b) aligned larger particles.

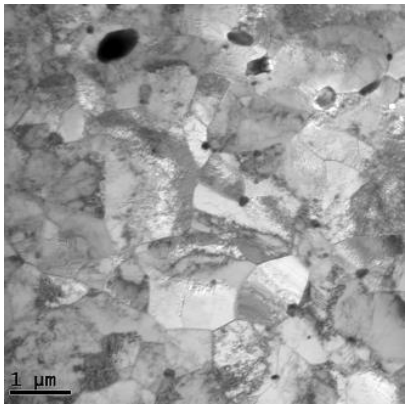

Figure 3. A bright field TEM image of APMT^{TM} rod showing fine (sub) grain structure.

4.2. Vickers microhardness results: Vickers microhardness of as received samples at room temperature was evaluated. The hardness was found to be 212±6 VHN in axial direction and 220±4 in the transverse direction. On the other hand, the hardness of APMT^{TM} steel was 307±7 VHN along the axial direction and 316±5 VHN in the transverse direction. The higher hardness of the APMT^{TM} steel compared to that of Fecralloy is likely due to the solid solution strengthening effect imparted by Mo and fine subgrain structure.

4.3. Tensile test results:

4.3.1. Tensile properties of Fecralloy: Figure 4 shows the engineering stress-strain curves of Fecralloy deformed at 10^{-3} s^{-1} at temperatures of 25, 200, 300, 400 and 500 ^{o}C. Serrations were observed in samples deformed at 300 and 400 ^{o}C. Figure 5 shows the engineering stress-strain curves of Fecralloy rods deformed at 300 ^{o}C at three different strain rates ($10^{-4,}$ 10^{-3} and 3×10^{-3} s^{-1}). The serrations are attributed to dynamic strain aging (DSA) which generally appear due to locking and unlocking of mobile dislocations by solute atoms. Given the amount of

substitutional solutes (Cr, Mo and Al) present in this steel, the role of substitutional solutes, if any, on the DSA effect needs to be understood.

Figure 6 shows the variation of yield strength, ultimate tensile strength and elongation to fracture of Fecralloy with temperature. The yield strength of the sample tested at room temperature is the highest (400 MPa). With increasing temperature the yield strength decreases progressively. However, in a certain temperature range (300 to 400 ^{o}C), the yield strength remains essentially constant, which is indicative of DSA. The ultimate tensile strength is also the highest at room temperature (583 MPa) and gradually decreases as the temperature increases. The elongation to fracture trend shows a minimum at 400 ^{o}C which corresponds to a temperature where serrated flow was observed. Even though the extent of the serrations was all through the plastic deformation stage at 300 ^{o}C, the elongation to fracture was the highest. The elongation to fracture value did decrease at 400 ^{o}C.

4.3.2. Nature of serrations in Fecralloy: Based on the nature of serrations, A-, B-, C- and D-type of serrations have been reported in earlier experiments with ferritic steels [7-9]. Type A serrations exhibit repeated initiation and continuous propagation of deformation bands along the specimen gage length. Sleeswyk [10] and McCormick [11] in their diffusion-controlled models of DSA attributed the occurrence of A-type serrations to diffusion of solute atoms to freely gliding dislocations. Sharp rise in load occurs when the solute locks dislocations, and the load drops when dislocations unlock from the solute atmosphere. Following A-type serrations, repeated locking and unlocking of dislocations due to highly mobile solutes lead to small B-type serrations about the mean level of loads in load-elongation curves. Type C serrations are oscillations of the load-elongation curve below the mean level of load. Type D serrations occur

as plateaus due to band propagation similar to Luders band with negligible work hardening or strain gradient ahead of the moving band front [12, 13]. While not shown here, APMT^{TM} also exhibited serrated flow in almost same temperature range as Fecralloy.

The engineering stress-strain curves of Fecralloy at 300 ^{o}C and 400 ^{o}C exhibited A and C type of serrations almost from the onset of plastic deformation. At 400 ^{o}C, serrations disappear after reaching the ultimate tensile stress. But at 300 ^{o}C, serrations are present throughout the plastic flow; the region after reaching the ultimate tensile stress shows B-type serrations. In Figure 5, the stress-strain curves at 300 ^{o}C for all strain rates exhibited dominance of A or A+C serrations before UTS, whereas at higher strains B-type serrations appeared.

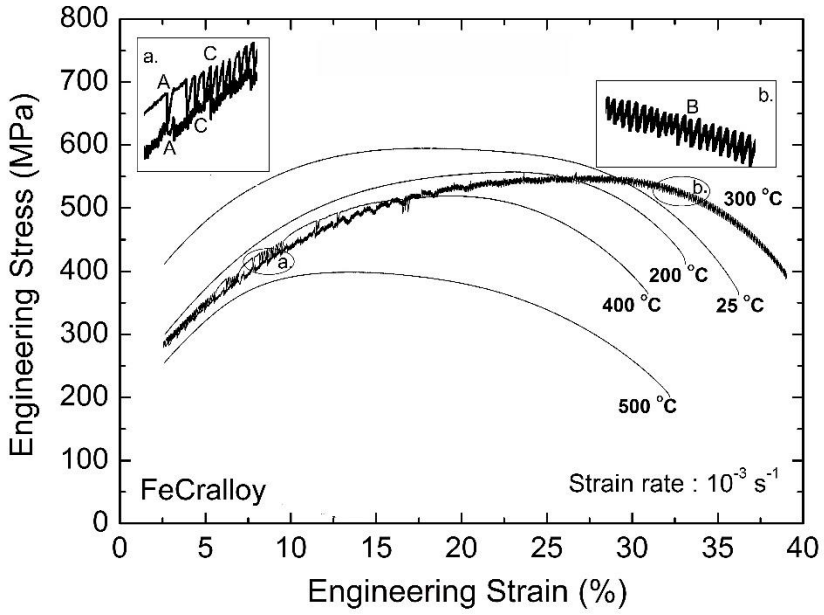

Figure 4. Engineering stress-strain curves at different temperatures and the strain rate of 10^{-3} s^{-1}

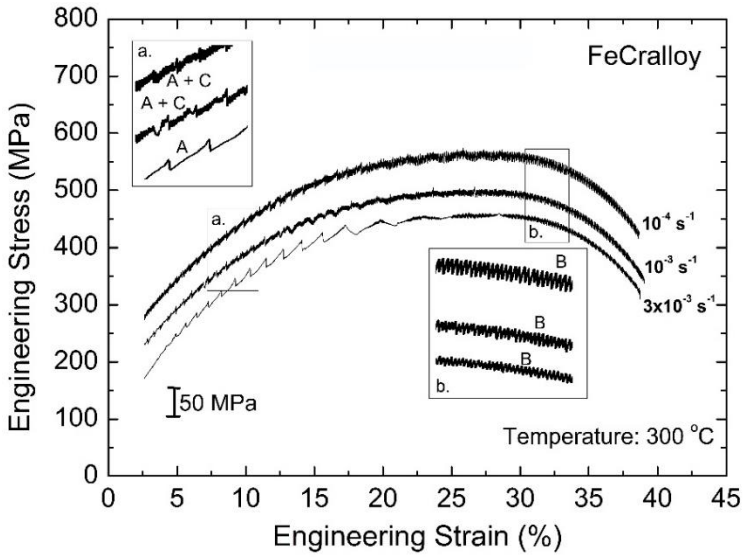

Figure 5. Engineering stress-strain curves for different strain rates at 300 °C. The curve of 10^{-3} s^{-1} is shifted by 50 MPa downward and that of 3×10^{-3} s^{-1} by 100 MPa to avoid overlapping of the curves.

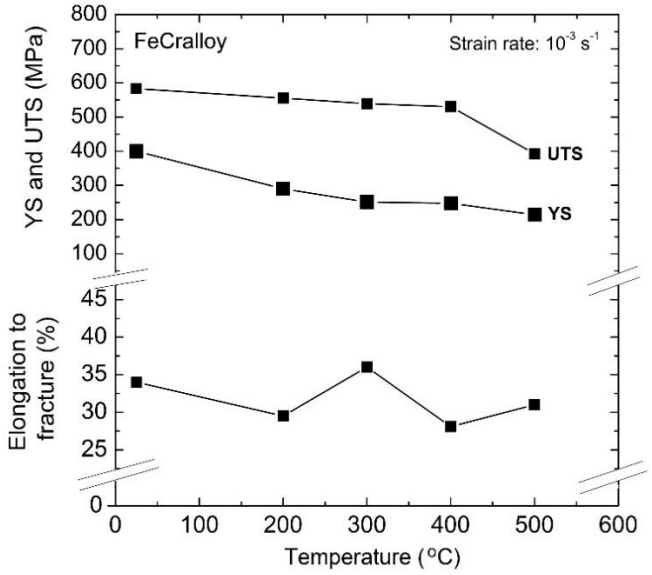

Figure 6. Variation of yield strength, ultimate tensile strength and elongation to fracture of Fecralloy rod as a function of temperature at a strain rate of 10^{-3} s^{-1}.

4.3.3. Comparison between properties of Fecralloy and APMT^{TM}: Table 1 lists tensile properties of Fecralloy in terms of yield strength, ultimate tensile strength and elongation to

fracture, which are compared with those of Kanthal APMT^{TM} rods deformed under somewhat similar testing conditions. It is noted that the yield strength and elongation to failure values remain almost constant with the variation of strain rate at a particular temperature for both the materials. At all temperatures (for 10^{-3} s^{-1} strain rate), the yield strength values of APMT^{TM} steel remained significantly higher than those of Fecralloy. At 300 ^{o}C and strain rate of

10^{-3} s^{-1}, Fecralloy and APMT^{TM} samples exhibited yield strengths about 600 MPa and about 250 MPa, respectively. If strength is a major criterion, APMT^{TM} is much superior. With regards to higher yield strength of APMT^{TM} alloy than that of Fecralloy, two main factors are most plausibly instrumental. Molybdenum imparts significant amount of solid solution strengthening in APMT^{TM}. In addition, the steel has a much fine (sub) grain size contributing to an extra amount of strengthening.

The variation of ultimate tensile strength against temperature exhibited a very similar trend as shown by yield strength. The ultimate tensile strength at room temperature was the highest for both steels. While for Fecralloy steel the ultimate tensile strength values gradually decreased, for APMT steel it started to decrease with increasing temperature albeit showed a positive variation as the temperature increased from 300 ^{o}C to 400 ^{o}C. At 300 ^{o}C at a strain rate of 10^{-3} s^{-1}, the ultimate tensile strength of APMT^{TM} was more than 700 MPa, while that for Fecralloy was around 550 MPa.

Table 1. Comparison of tensile properties of Fecralloy and APMT^{TM} rods

Material (Strain Rate (s^{-1}))	Temperature of Tensile Test (^oC)	Yield Strength (MPa)	Ultimate Tensile Strength (MPa)	Elongation to Fracture (%)
FeCralloy (10^{-3})	25	400	583	34.0
	200	290	555	29.5
	300	251	539	36.0
	400	248	517	28.1
	500	214	392	31.0
APMT (10^{-3})	25	682	750	26.0
	200	657	747	23.0
	300	597	727	25.4
	400	632	738	22.0
	500	585	651	25.0
FeCralloy rod (3×10^{-3})	300	254	548	36.0
APMT rod (3×10^{-3})	300	605	745	23.0
FeCralloy rod (10^{-4})	300	260	564	36.0
APMT rod (10^{-4})	300	600	740	22.5

Fecralloy exhibited more sustained strain hardening capability compared to APMT^{TM} resulting in higher ductility. Ductility in terms of elongation to fracture values for Fecralloy was found to be consistently higher than APMT^{TM} steel. The larger inclusions present in the microstructure did not act as flaw nucleation sites contributing to any premature failure during the course of tensile testing.

4.4. Fractography: Figure 7 shows a number of SEM fractographic images of three tensile specimens tested at three different temperatures but at the same strain rate of 10^{-3} s^{-1}. Figures 7a and b show the low-magnification and high-magnification SE images of fracture surface of tensile specimen of Fecralloy tested at room temperature. The fracture mode was essentially ductile. The tensile fracture behavior examined for the range of temperatures and strain rates revealed that the fracture mode remained transgranular and ductile with characteristic dimple

features. The fracture surfaces of room temperature specimen at low magnification displayed a star-like appearance while a typical cup and cone fracture at intermediate (Figures 7c and 7d) and high temperatures (Figures 7e and 7f) were detected. The fracture mode was characterized by dimples resulting from coalescence of microvoids for all test temperatures. The size of equiaxed dimples increased with increase in temperature, indicating dominance of void growth process at elevated temperatures.

5. Conclusion: The work primarily focused on evaluation of tensile properties of Fecralloy and APMT^{TM} steel along with microstructural characteristics and Vickers microhardness. It was shown that the tensile yield strength, ultimate tensile strength and elongation to fracture values over the temperature range of interest (25-500 ^{o}C) are reported. The DSA effect was noted from the serrations of the stress-strain curves. The superior strength of APMT^{TM} compared to Fecralloy was attributed to mainly two factors – solid solution strengthening imparted by higher Mo content (3 wt.%) and (sub)grain strengthening effect due to fine subgrain structure (1-3 μm), respectively. Although this study does not take into account any long term effect on microstructure and mechanical properties, aluminum-bearing ferritic steels should be analyzed carefully.

Acknowledgement: The research was performed using funds received from the DOE Office of Nuclear Energy's Nuclear Energy University Programs (NEUP). We would also like to acknowledge the help provided by Drs. Somayeh Pasebani and Sultan Alsagabi with some experiments.

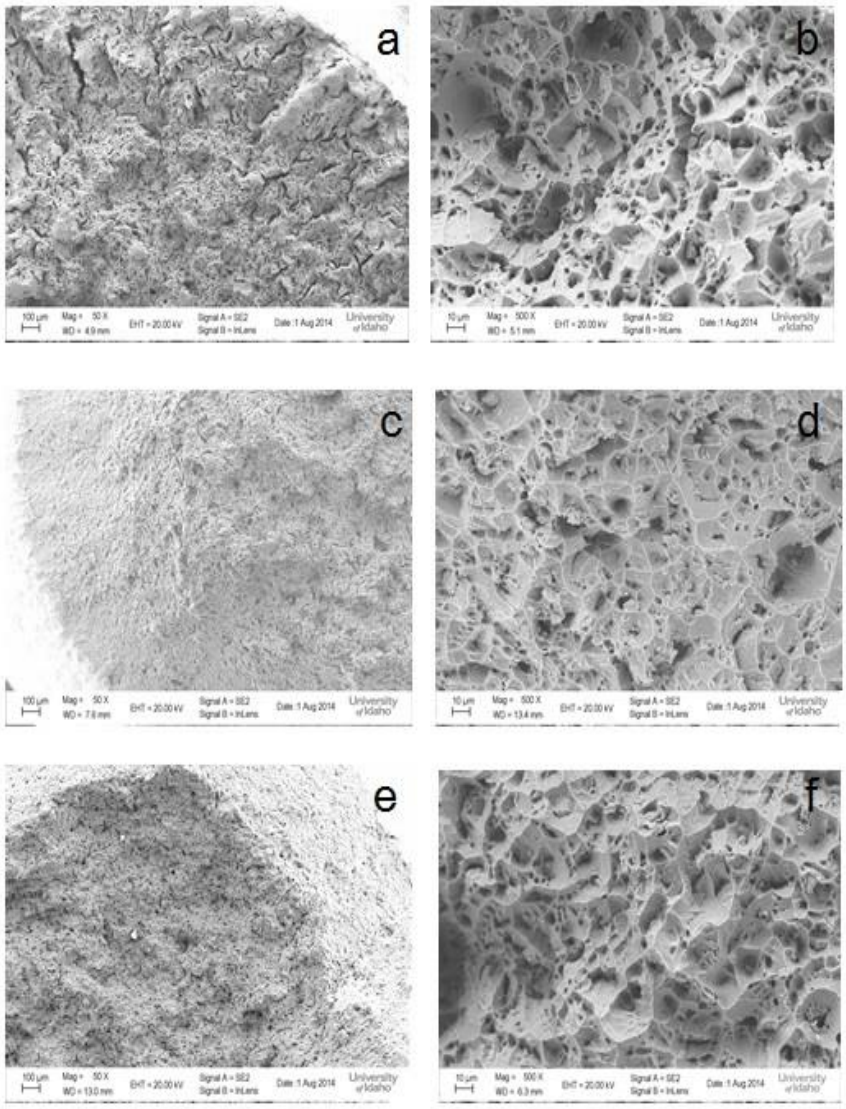

Figure 7. Scanning electron microscopy secondary electron images showing fracture surface features of Fecralloy rod tensile tested at: (a) and (b) room temperature, (c) and (d) 300 ºC, (e) and (f) 500 ºC.

References:

1. K.L. Murty and I. Charit, J. Nucl. Mater. 383 (1-2) (2008) 189-195.

2. S.J. Zinkle, K.A. Terrani, J.C. Gehin, L.J. Ott and L.L. Snead, J. Nucl. Mater. 448 (2014) 374-379.

3. K.A. Terrani, S.J. Zinkle and L.L. Snead, J. Nucl. Mater. 448 (2014) 420-435.

4. B.A. Pint, K.A. Terrani, M.P. Brady, T. Cheng and J.R. Keiser, J. Nucl. Mater. 440 (2013) 420-427.

5. B. Petrovic, Nucl. Eng. Int. March (2014) 26-29.

6. Bo Jonsson, Roger Berglund, Jonas Magnusson, Peter Henning, Mats Hattestrund, Mater. Sci. Forum Vols. 461-464 (2004) 455-462.

7. B.K. Choudhary, K.B.S. Rao, S.L. Mannan, Int. J. Pres. Vessels Pip. 58 (1994) 151–160.

8. B.K. Choudhary, K.B.S. Rao, S.L. Mannan, B.P. Kashyap, Mater. Sci. Technol. 15 (1999), 791–97.

9. R.K. Upadhaya, M.N. Shetty, Z. Metallkd. 82 (1991) 19–21.

10. A.W. Sleeswyk, Acta Metall. 6 (1958) 598–603.

11. P.G. McCormick, Acta Metall. 20 (1972) 351–354.

12. P. Rodriguez, Bull. Mater. Sci. 6 (1984) 653–63.

13. S.C. Tjong, S.M. Zhu, Metall. Mater. Trans. 28A (1997) 1347–1355.